18

Stellar rotation

In this chapter, we concern ourselves primarily with the spectroscopic effects of stellar rotation, including the line broadening caused by rotation, techniques for extracting the rotation rate from the broadening, and some of the results. Many of the analysis tools are the same as those discussed in Chapter 17.

Stellar rotation is the driving force for diverse phenomena in stellar atmospheres such as circulation currents, mass loss, and magnetic field generation and its offshoots: starspots, flares, chromospheres and coronae, and activity cycles. The existence of stellar rotation comes as no surprise. Since we believe stars form out of interstellar clouds, and clouds collide with one another and are subject to other torques such as those induced by galactic rotation, we would predict rather large stellar rotation on the basis of the conservation of angular momentum. Moment of inertia scales roughly as the square of the linear dimension. With 44 million solar radii per parsec, cloud rotation should be magnified by something like 15 orders in coming to stellar dimensions. Some stars rotate near the "break-up" velocity, where the gravitational acceleration is comparable to the centripetal force at the equator, but even these rates are small compared to what is expected. Apparently dissipation of angular momentum is an integral part of star formation.

The Sun's rotation, first measured in the early 1600s by Galileo, is very slow, amounting to only 2.0 km/s (sidereal; 1.86 km/s synodic) at the equator. Such slow rotation rates are typical of cool stars. The Sun also shows differential rotation, with the equator having an angular velocity about 25% larger than at higher latitudes $\approx 75°$.

The effects of rotation on the continuous spectrum are small except when rotation is very near the break-up rate. The spectral lines, on the other hand, are strongly changed by the relative Doppler shifts of the light coming from different parts of the stellar disk. The approaching limb corresponds to the short-wavelength portion of a rotation-broadened line profile and the receding
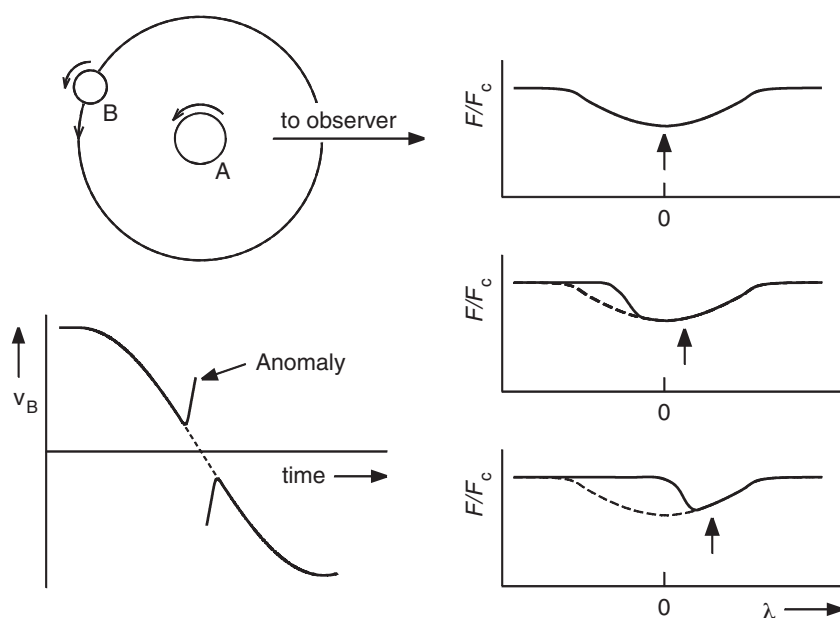
458

Fig. 18.1.   The radial-velocity anomaly occurs when low spectral resolution is used to measure the radial velocity of rotating eclipsing stars. The spectral lines of the B component disappear starting on the short-wavelength side as the disk of the star is covered during ingress into the eclipse. This gives the impression of a line shift.

limb to the long-wavelength portion. Indeed, the line profile becomes a one-dimensional map of the stellar disk through the one-to-one coupling of position on the stellar disk and Doppler shift within the profile. This point was instrumental in the early proofs that stars rotate, namely the eclipsing binary observations consisting of radial velocity measurements as a function of time (McLaughlin 1924, Rossiter 1924, Shajn & Struve 1929). The orbital radial velocity is expected to go through zero during eclipse when the motion is across our line of sight, but the observations showed a steep rise between first and second contact, and the inverse behavior between third and fourth contact. Figure 18.1 illustrates the effect. Part way through eclipse, the *observable portion* of the star being eclipsed has a net velocity due to rotation that is away from the observer. The remainder of the line is missing because it comes from the hidden portion of the partially eclipsed star. Hence the line appears red-shifted. Upon egress, the blue-shifted portion of the profile is seen. The resolution of these early spectrograms was too low for changes in line shape to be discerned, so the lines appeared to show a shift in position that the observers translated into radial velocity.

The Doppler line broadening from rotation depends on the orientation of the axis of rotation relative to the line of sight. We expect a wide range in line broadening corresponding to the maximum for equator-on objects and to zero for the pole-on objects. The apparent distribution of observed rotation rates will reflect this projection effect in combination with the true distribution of rotation rates.

Photometric measurements also deliver rotation information whenever large-scale non-uniformities exist on the surface of a star. Each time the star rotates, we see a rough longitude map of the surface brightness as a time series in the photometry. In its simplest form, a single large surface feature introduces a once-per-revolution modulation in the brightness, thus supplying us with the rotational period. The inclination of the rotational axis is also important here since stars seen near pole-on will show no modulation. This same phenomenon actually occurs within line profiles, allowing us to map the stellar surface.

Stellar rotation rates are specified using the projected equatorial velocity, $v \sin i$, for spectroscopic observations, or the period for modulation observations. Several catalogues have been compiled, e.g., Boyarchuk and Kopylov (1964), Bernacca and Perinotto (1970–71), and Uesugi and Fukuda (1982). Catalogues are valuable tools when properly used. However, some considerable care should be exercised since the tabulated data often includes a wide range of observing technique, equipment, accuracy, and lower limit of detection. Most older catalogues are limited to $v \sin i \gtrsim 25$ km/s, which is simply the resolution limit, meaning that the star rotates too slowly to be measured with the equipment they used. In some cases, this resolution limit is listed as $v \sin i$. The actual rate of rotation is usually much smaller than such catalogue entries, as shown by modern high-resolution work.

Reviews on stellar rotation have been written by Kraft (1970), Moss and Smith (1981), and Slettebak (1985). See also Catalano and Stauffer (1991). The rotation of the Sun is reviewed by Howard (1984). A comprehensive theoretical treatise on rotation has been written by Tassoul (1978).

Once again notice that the symbol $\Delta\lambda$ is used to mean distance from the central position of a spectral line and is usually expressed in velocity units rather than length units.

The Doppler-shift distribution

The shape of most photospheric spectral lines is basically the shape of the Doppler-shift distribution, i.e., the fraction of starlight at each Doppler shift. Although this was covered in considerable detail in Chapter 17, the concept is so fundamental, it bears repeating. Essentially every element of surface from
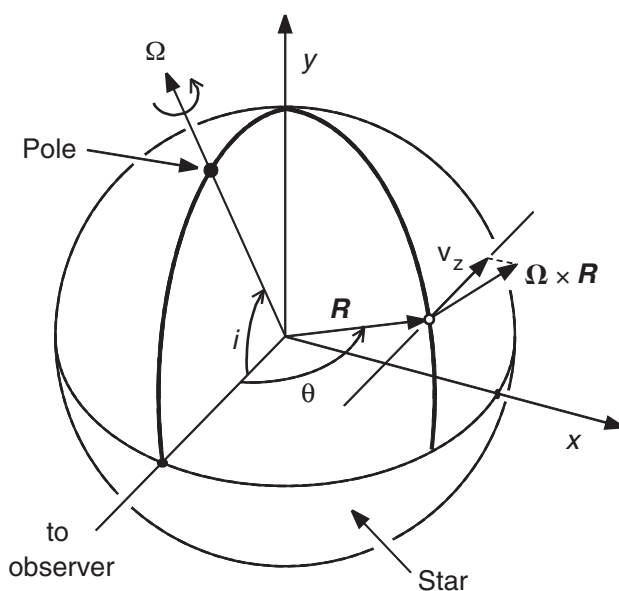
Fig. 18.2. The rotation axis is inclined at an angle i to the line of sight along the z axis. The axis is chosen to make $\boldsymbol{\Omega}$ lie in the y–z plane. For some arbitrary point on the surface at an angle θ from the line of sight, the velocity is $\boldsymbol{v} = \boldsymbol{\Omega} \times \boldsymbol{R}$, where $\boldsymbol{R}$ is the stellar radius. The z component of this velocity gives the Doppler shift.

which light comes to us is moving relative to the center of mass of the star. The motions arise primarily from photospheric velocities such as granulation and oscillations, and from rotation of the star. The line-of-sight components of these velocities, integrated over the apparent disk of the star, is the Doppler-shift distribution. In the common case, the absorption lines in the spectrum of a star are inverted images of this distribution, scaled to the position and equivalent width of the real line. This is none other than the convolution of the Doppler-shift distribution with the thermal profile, as expressed in Eq. (17.14).

In this chapter we focus on the rotation component of Eq. (17.14), first when the rotation is large compared to other velocities, and second when it is not.

The rotation profile

The Doppler-shift distribution from rotation has a characteristic shape that we now calculate. This is the shape taken on by spectral lines when rotation far surpasses the other Doppler shifts. The star is assumed to be spherical and to rotate as a rigid body. We choose the coordinate arrangement shown in Fig. 18.2. The axis of rotation lies in the y–z plane. The x–y plane is perpendicular to the line of sight along the z axis. The angle of inclination, i, is

measured from the z axis to the axis of rotation. We call the vector angular velocity of rotation $\boldsymbol{\Omega}$. Then the linear velocity of any point on the surface of the stars is the vector $\boldsymbol{v}$ given by

$$\boldsymbol{v} = \boldsymbol{\Omega} \times \boldsymbol{R},$$

where $\times$ means vector product and $\boldsymbol{R}$ is the radius vector as shown in Fig. 18.2. The Doppler shift arises from the z component of the vector product, namely, $y\Omega_x - x\Omega_y$, but there is no x component of Ω by choice of the coordinate arrangement, so $\Omega_x = 0$. Since the y component is $\Omega_y = \Omega \sin i$, the z component of velocity becomes

$$v_z = x\Omega \sin i. \tag{18.1}$$

We think of v_z as the $\Delta\lambda$ shift from line center expressed in kilometers per second (which could be converted to angstroms by multiplying by λ/c, but then the scale of the broadening would change from one spectral line to the next). This $\Delta\lambda$ was called $\Delta\lambda_R$ in Eq. (17.9). Equation (18.1) is an important relation because it shows that all elements on the stellar surface having the same x coordinate also show the same wavelength displacement due to rotation. We can then imagine the stellar disk being divided into strips as shown in Fig. 18.3. The Doppler shift is nearly constant along each strip and becomes exactly so in the limit. The largest shift occurs at the limbs where $x = R$, and has a value

$$v_L = R\Omega \sin i = v_{eq} \sin i, \tag{18.2}$$

where v_{eq} is the equatorial rotation velocity. We frequently omit the subscript on v_{eq} when there is no ambiguity, writing simply $v\sin i$.

The flux for such a star is still given by Eq. (5.5),

$$\mathfrak{F}_\nu = \oint I_\nu \cos\theta \, d\omega, \tag{18.3}$$

but now I_ν is Doppler shifted according to Eq. (18.1). (If you have not already read Chapter 17, you may wish to look over the material associated with Eq. 17.9.) Take $d\omega = dA/R^2$, where dA is an increment of surface area on the star of radius R. Then the increment of area on the apparent disk of the star, using the coordinates of Fig. 18.2, is $dx\,dy = dA\cos\theta$ so that

$$\mathfrak{F}_\nu = \iint I_\nu \frac{dx\,dy}{R^2}. \tag{18.4}$$

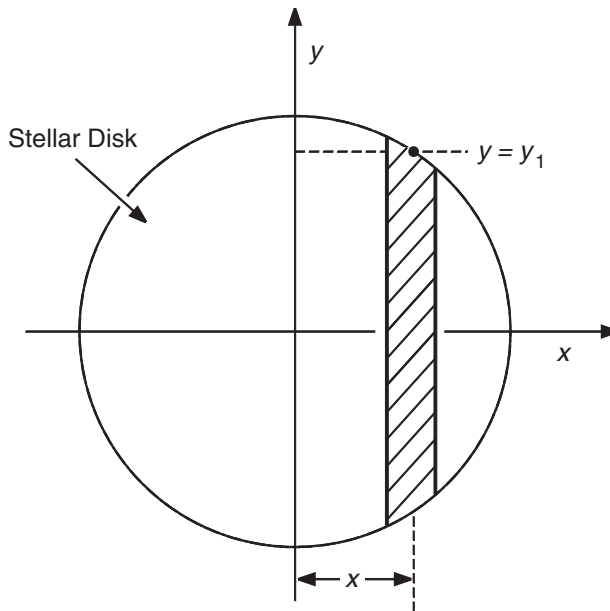The integration is carried out over the apparent stellar disk.

Fig. 18.3. The apparent disk of the star can be thought of as a series of strips parallel to the projected rotation axis, each having a Doppler shift proportional to x according to Eq. (18.1). The amount of light at this Doppler shift varies with the length of the strip, from $-y_1$ to $+y_1$, which for a circular disk is given by Eq. (18.9).

The most general and fundamental procedure is to calculate I_ν at many points on the disk (using a model photosphere), and obtain $\mathfrak{F}_\nu$ numerically. This scheme has the advantages that limb darkening is automatically taken into account, one can incorporate center-to-limb variations in the I_ν line profile, and non-rigid rotation can be introduced. It has the disadvantages of being a great deal of computational work and, to a certain degree, masking the behavior of the physical process. The less general analytical development assumes that any variation in the shape of the I_ν profile across the stellar disk is negligible compared to the rotational broadening, and proceeds as follows. Define the intrinsic line profile at any point on the disk to be $H(\Delta\lambda) = H(\nu) = I_\nu/I_c$, that is, the ratio of intensity at any point in the spectrum to the continuum intensity. The flux profile in a non-rotating star can then be written as

$$\frac{\mathfrak{F}_\nu}{\mathfrak{F}_c} = \frac{\oint H(\nu)\, I_c \cos\theta\, d\omega}{\oint I_c \cos\theta\, d\omega} \ . \tag{18.5}$$

If $H(v)$ were completely independent of position on the disk, $H(v)$ could be factored out and Eq. (18.5) would become

$$\mathfrak{F}_v/\mathfrak{F}_c = H(v), \tag{18.6}$$

i.e., $H(v)$ would be the flux profile as well as the specific-intensity profile. But in the case of a rotating star, $H(v)$ depends on disk position through the Doppler shifts according to Eq. (18.1). Therefore,

$$\mathfrak{F}_v = \oint H(v - v_z) I_c \cos\theta \, d\omega. \tag{18.7}$$

For the Sun, center-to-limb variations in the actual *shape* of $H(v)$ are $\approx 25\%$, or less than a few km/s. By comparison, rotation is often tens or hundreds of km/s. In such cases, we can neglect any changes in the strength or shape of $H(v)$ and include only the v_z translations.

Next, convert Eq. (18.7) into the form of Eq. (18.4) to obtain

$$\mathfrak{F}_v = \iint H(v - v_z) I_c \frac{dx\,dy}{R^2}. \tag{18.8}$$

Then put in the integration limits: x running from $-R$ to $+R$ and y from $-y_1$ to $+y_1$, where

$$y_1 = (R^2 - x^2)^{1/2} = R\left[1 - \left(\frac{v_z}{v_L}\right)^2\right]^{1/2}. \tag{18.9}$$

We then have

$$\mathfrak{F}_v = \int_{-R}^{R} H(v - v_z) \int_{-y_1}^{y_1} I_c \frac{dy}{R} \frac{dv_z}{v_L}. \tag{18.10}$$

We now define $G(\Delta\lambda)$ to be the y integration in Eq. (18.10) combined with the denominator of Eq. (18.5),

$$G(\Delta\lambda) = G(v_z) = \frac{1}{v_L} \frac{\int_{-y_1}^{y_1} I_c \, dy/R}{\oint I_c \cos\theta \, d\omega} \quad \text{for} \quad |v_z| \leq v_L \quad \text{or} \quad |\Delta\lambda| \leq \Delta\lambda_L$$

$$= 0 \quad\quad\quad\quad\quad\quad \text{for} \quad |v_z| > v_L \quad \text{or} \quad |\Delta\lambda| > \Delta\lambda_L. \tag{18.11}$$

The normalized line profile can then be written as

$$\mathfrak{F}_v/\mathfrak{F}_c = \int_{-\infty}^{\infty} H(v - v_z)\, G(v_z)\, dv_z$$
$$= H(v) * G(v_z)$$
$$= H(\Delta\lambda) * G(\Delta\lambda). \tag{18.12}$$

This convolution is an interesting and powerful result. It says that as long as $H(\Delta\lambda)$ has the same shape over the disk of the star, we can take the flux profile, as per Eq. (18.6), for a non-rotating star and convolve it with the rotation profile, $G(\Delta\lambda)$, to obtain the rotational broadened flux profile. The larger the rotation rate, the wider $G(\Delta\lambda)$ is compared to $H(\Delta\lambda)$, and the more the flux profile looks like $G(\Delta\lambda)$. The purest case is when $H(\Delta\lambda)$ is a delta-function, for then it becomes nothing more than a marker of Doppler shifts. The convolution does essentially three things: it shifts $G(\Delta\lambda)$ to the position of the observed stellar line, it scales $G(\Delta\lambda)$ from unit area to the equivalent width of the stellar line, and it turns $G(\Delta\lambda)$ up-side-down (when the stellar line is a normal absorption line).

We can evaluated $G(\Delta\lambda)$ without excessive error by the linear limb darkening law, Eq. (17.11),

$$I_c/I_c^0 = (1 - \varepsilon) + \varepsilon \cos\theta, \qquad (18.13)$$

where I_c^0 is the specific intensity at the center of the disk and θ is the usual angular limb distance. As we saw in Fig. 17.6, the limb-darkening coefficient ε is a slowly varying function of λ, and is therefore taken to be constant over a line profile. The analytical integration of $\oint I_c \cos\theta \, d\omega$ in the denominator of Eq. (18.11) then gives $\pi I_c^0 (1 - \varepsilon/3)$. In the numerator of $G(\Delta\lambda)$ we have

$$\int_{-y_1}^{y_1} I_c \, dy/R = \frac{2I_c^0}{R} \int_0^{y_1} [(1 - \varepsilon) + \varepsilon \cos\theta] \, dy$$

$$= \frac{2I_c^0(1 - \varepsilon)y_1}{R} + \frac{2\varepsilon I_c^0}{R} \int_0^{y_1} \cos\theta \, dy.$$

Using $\cos\theta = [R^2 - (x^2 + y^2)]^{1/2}/R$ as shown in Fig. 18.4, and the fact that $\int (A^2 - y^2)^{1/2} \, dy = \frac{1}{2}[y(A^2 - y^2)^{1/2} + A^2 \sin^{-1}(y/A)]$, we obtain

$$\int_{-y_1}^{y_1} I_c \frac{dy}{R} = 2I_c^0(1 - \varepsilon)[1 - (v_z/v_L)^2]^{1/2} + \frac{1}{2}\pi\varepsilon I_c^0[1 - (v_z/v_L)^2].$$

And finally,

$$G(\Delta\lambda) = G(v) = \frac{2(1 - \varepsilon)[1 - (v_z/v_L)^2]^{1/2} + \frac{1}{2}\pi\varepsilon[1 - (v_z/v_L)^2]}{\pi v_L(1 - \varepsilon/3)}$$

$$= c_1[1 - (\Delta\lambda/\Delta\lambda_L)^2]^{1/2} + c_2[1 - (\Delta\lambda/\Delta\lambda_L)^2], \qquad (18.14)$$

where the constants have been lumped together into c_1 and c_2. As before, $\Delta\lambda_L$ and v_L are the maximum shifts, corresponding to the disk points on the limb at
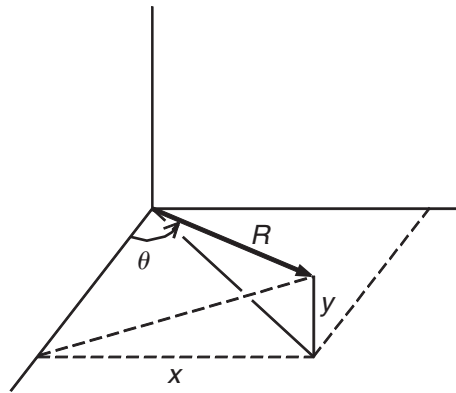
Fig. 18.4.   We express $\cos\theta$ in terms of the x, y, and R coordinates of the point on the surface of the star.

the equator as per Eq. (18.2). The argument $v_z/v_L = \Delta\lambda/\Delta\lambda_L = x/R$ is unitless so the wavelength shifts can be expressed in any units, usually kilometers per second or angstroms.

Figure 18.5 is a graph of the two parts of $G(\Delta\lambda)$ and their sum with $\varepsilon = 0.6$. If $\varepsilon = 0$, which means a uniformly illuminated stellar disk, the second part of the rotation function is zero. The first term alone is the equation for an ellipse. If $\varepsilon = 1$, we say that the disk is "fully darkened." Then only the second term in Eq. (18.14) remains, and it has a parabolic shape. Usually ε is chosen on the basis of model photospheres, by means of a grid like the one in Fig. 17.6 of the last chapter, and the details obviously depend on $T(\tau_0)$ as per the discussion in Chapter 9.

Sometimes a model photosphere is used to generate $H(\Delta\lambda)$. In other cases $H(\Delta\lambda)$ is taken to be an observed profile from a narrow-lined star (e.g., Sabby & Lacy 2003). The handling of $H(\Delta\lambda)$ becomes important for slow rotation rates where it is necessary to account for the broadening of macroturbulence and for high rotation where strong variations can occur across the stellar surface. This problem has been studied by Collins and Truax (1995).

Theoretical line profiles are shown as a function of $v\sin i$ in Fig. 18.6. Notice how the original profile becomes very shallow with the larger rotation. The equivalent width of the line is conserved according to Theorem 6 of Chapter 2. This is also clear from physical considerations. Since I_ν as emitted at any spot on the stellar surface is a complete spectrum, independent of the rest of the star, Doppler shifting each I_ν spectrum cannot cause the total absorption in a line to increase or decrease. Figures 18.7 and 18.8 show how
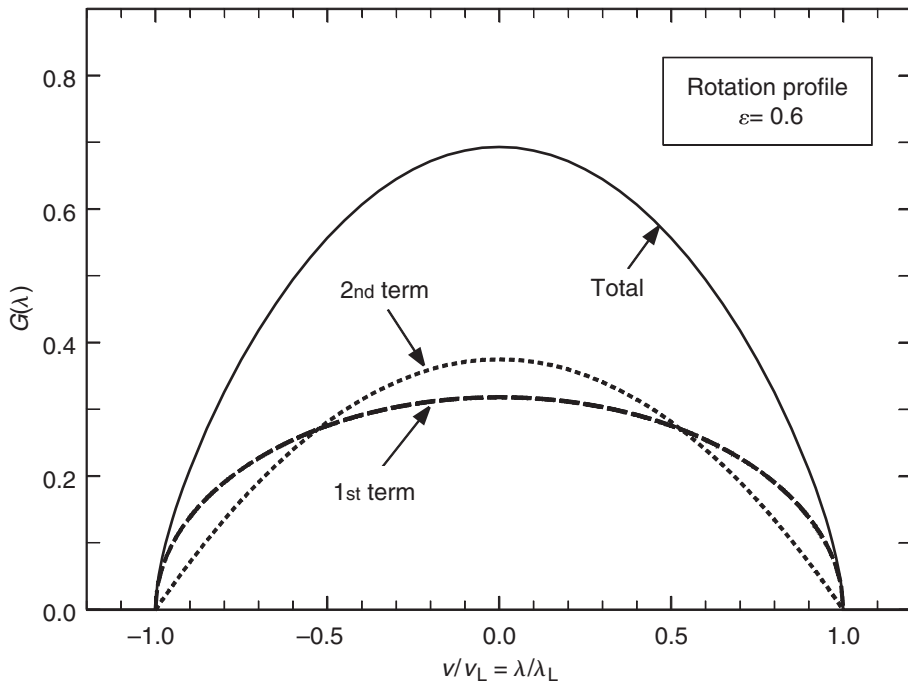
Fig. 18.5. The rotation profile, Eq. (18.14), is shown by the solid line for $\varepsilon = 0.6$ and labeled "total." It is the sum of the "1st term" and "2nd term" curves.

rotational broadening looks in real spectra. We see striking changes in the profile shapes. As expected, all of the lines are wider and shallower, and there is increased blending.

Profile fitting for $v \sin i$

The projected equatorial velocity, $v \sin i$, can be established by comparing the line profiles of the star to computed rotation profiles of the type discussed in the last section. The lines chosen should be free of strong pressure broadening, and yet must be strong enough so the rotation-broadened profile can still be seen and measured. In hot stars, there are relatively few lines that are suitable. The lines He I $\lambda4026$, $\lambda4388$, and $\lambda4471$ have commonly been used in hot stars even though the third line has a substantial blend. For slightly cooler stars, the late B through early A types, the Mg II $\lambda4481$ line is nearly ideal as long as the rotational broadening is large compared to the 0.2 Å (13 km/s) splitting of this doublet. In A and F spectral types, Fe I $\lambda4405$,
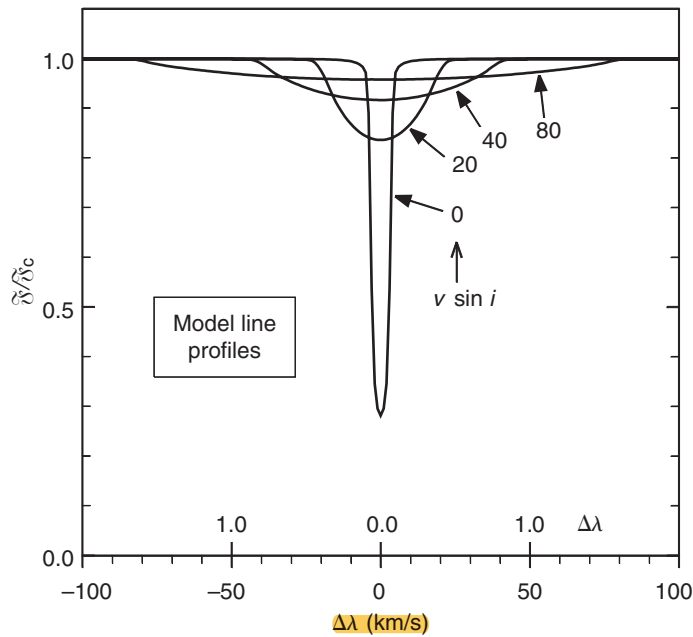
Fig. 18.6.   Computed profiles illustrate the broadening effect of retation. The profiles are labeled with $v \sin i$ in km/s. The equivalent width is conserved.

$\lambda 4473$, $\lambda 4476$, $\lambda 4549$, and Fe II $\lambda 4508$ were often chosen in days past. Lines at longer wavelengths can now also be measured routinely thanks to the advent of red-sensitive detectors. This is important for the cool stars where the serious problem of line blending can be ameliorated by observing in the red, typically between 6000 and 6500 Å, but as we see in Fig. 18.8, the problem never goes away.

Examples of the fitting of line profiles can be seen in numerous papers, e.g., Elvey (1929), Struve (1930), Slettebak (1954), Abt (1957), Smith and Gray (1976), Hill (1995), Johns-Krull (1996), and Chauville *et al.* (2001). Figure 18.9 shows an early analysis of $\lambda 4508$ in ν Per (F5 II), where the profile is matched within errors by a rotation profile having $v \sin i = 46$ km/s. Another example is shown in Fig. 18.10. Here we see that the corners of the rotation profile have been smoothed away. The presence of macrotubulence accounts for this, although blending with nearby lines also occurs. Synthesis of a whole spectral interval is an elaboration of the profile-fitting method. Macroturbulence and the thermal profile can be included explicitly in the computed spectrum.
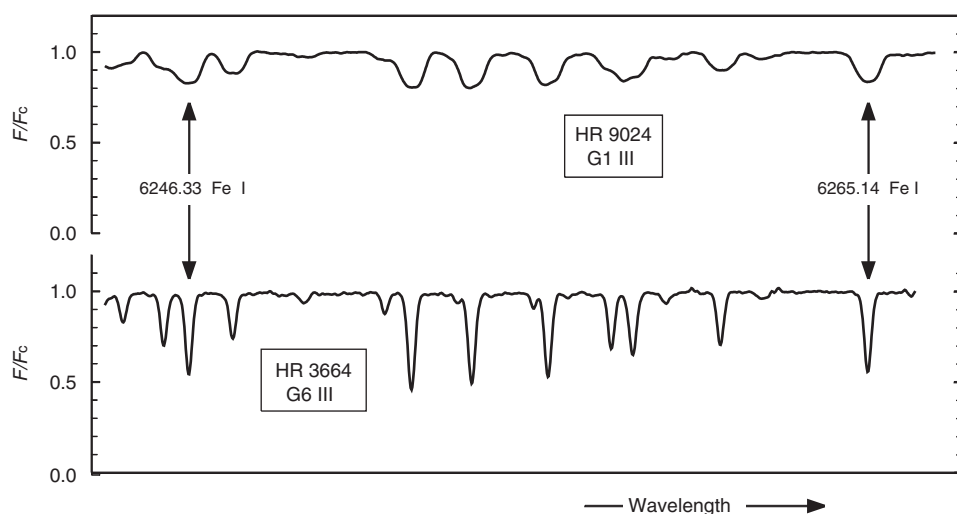
Fig. 18.7.   These two G giants illustrate the Doppler broadening of the line profiles by rotation. HR 3664 shows low rotation, comparable to the macro-turbulence broadening, of a few km/s, while HR 9024 shows rotational broadening that is substantially larger. Data taken at the Elginfield Observatory.
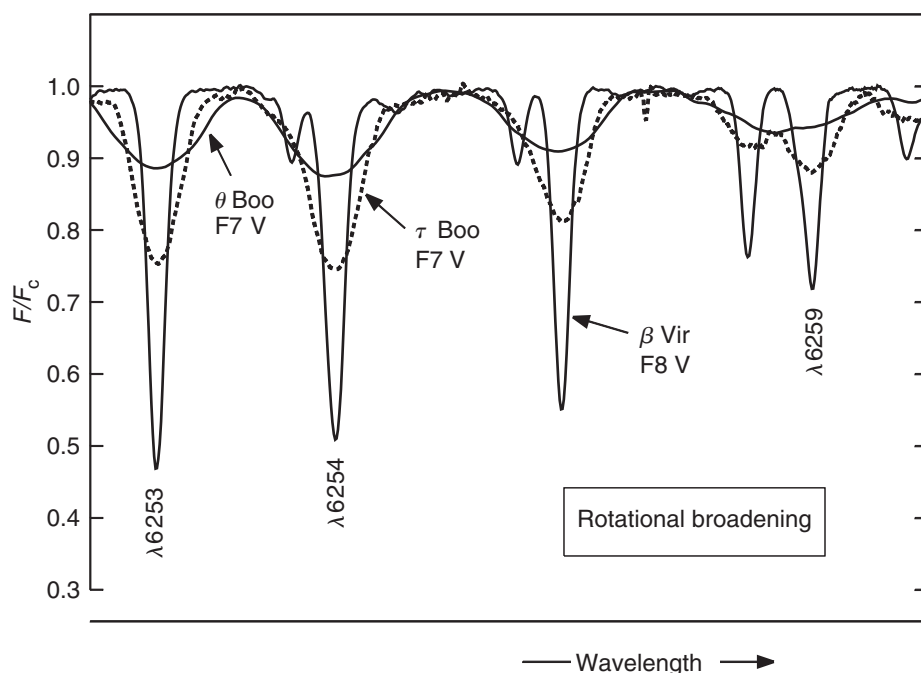

Fig. 18.8.   The rotational broadening in three F dwarfs are compared. Data from the Elginfield Observatory.
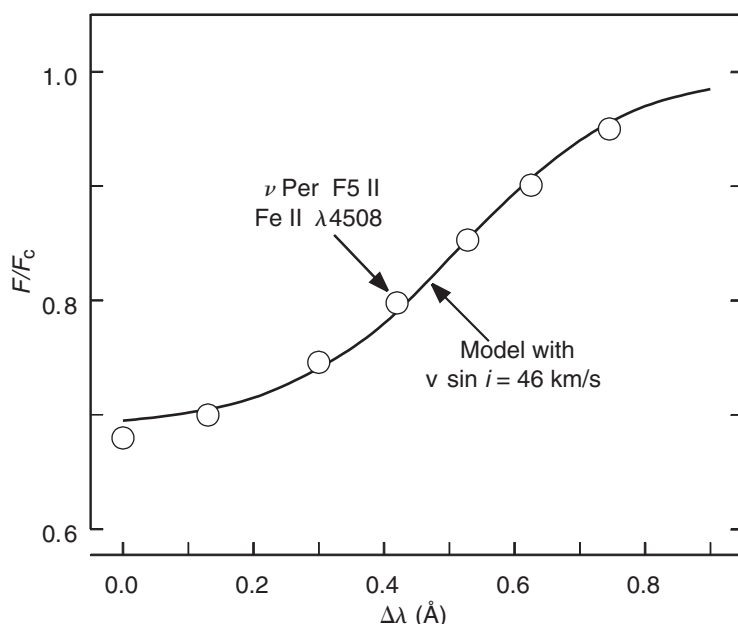
Fig. 18.9   This profile of Fe II λ4508 in ν Per is matched to a rotation profile having $v\sin i = 46$ km/s. Adapted from Abt (1957) with permission of the Astrophysical Journal, copyright 1957 by the University of Chicago Press.

Profile width as a measure of $v \sin i$

Although reasonable agreement was found between theory and observation in the early investigations, it was soon realized that the resolution on many spectrograms was sufficient to determine only the lower Fourier components of the profile. Furthermore, $G(\Delta\lambda)$ scales with $v\sin i$, so it was assumed that only one parameter *needed* to be measured. Consequently, the half-width of the profile was often adopted as the single parameter used to measure $v\sin i$. The saving of labor makes statistical studies of rotation easier and quicker even though the ultimate in precision is compromised. A series of standards is first set up. Line widths were then estimated by eye directly from the spectrograms in days of yore, or from graphs of the profiles in more recent work. An extension of this is to cross-correlate a large portion of the stellar spectrum with a narrow-lined standard and use the width of the correlation peak.

The stars measured by Slettebak (1954, 1955, 1956), Slettebak and Howard (1955), and Slettebak *et al*. (1975) were often adopted as standards. Several more recent calibrations have also followed this same approach, e.g., Abt and
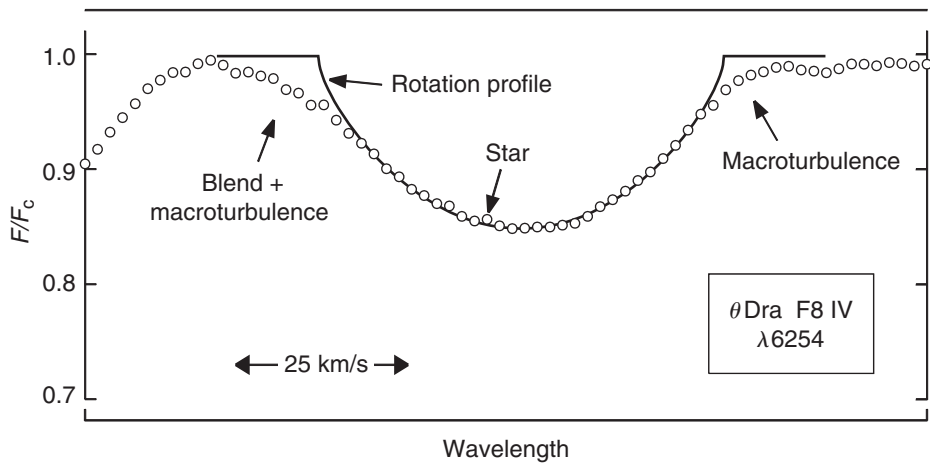
Fig. 18.10.   An observed profile of θ Dra is compared to the classic rotation profile. The rotation profile shows sharp corners where it joins the continuum. The high Fourier frequencies needed to form these corners are filtered away by other broadeners, in this case macroturbulence of several km/s. Data from the Elginfield Observatory.

Morrell (1995), Penny (1996), Fekel (1997, 2003), De Medeiros and Mayor (1999), Abt *et al.* (2002), and Mochnacki *et al.* (2002).

Problems with width measurements occur at both high and low rotation rates. At high rotation rates ($v \sin i \gtrsim 200$ km/s), gravity darkening, significant variations in $H(\Delta\lambda)$ across the stellar disk, and non-spherical stars introduce more parameters and these simply cannot be described by one measurement. With low rotation ($v \sin i \lesssim 20$ km/s), other sources of broadening become competitive with rotation, especially turbulence and finite instrumental resolution. In both extremes, reliance on a width parameter must be abandoned and the profile must be analyzed in detail.

Fourier analysis for large $v \sin i$

The information contained in the rotational broadening is more favorably distributed in the Fourier domain than in the wavelength domain. Figure 18.11 show the transform of $G(\Delta\lambda)$, which we call $g(\sigma)$, and its lobe structure. The first sidelobe has an amplitude of about one-tenth of the main lobe, and is negative in sign. The sidelobes alternate in sign and slowly diminish in amplitude as shown in the figure. The horizontal scale of the rotation profile is proportional to $v \sin i$, so of course the scale of $g(\sigma)$ is inversely proportional to
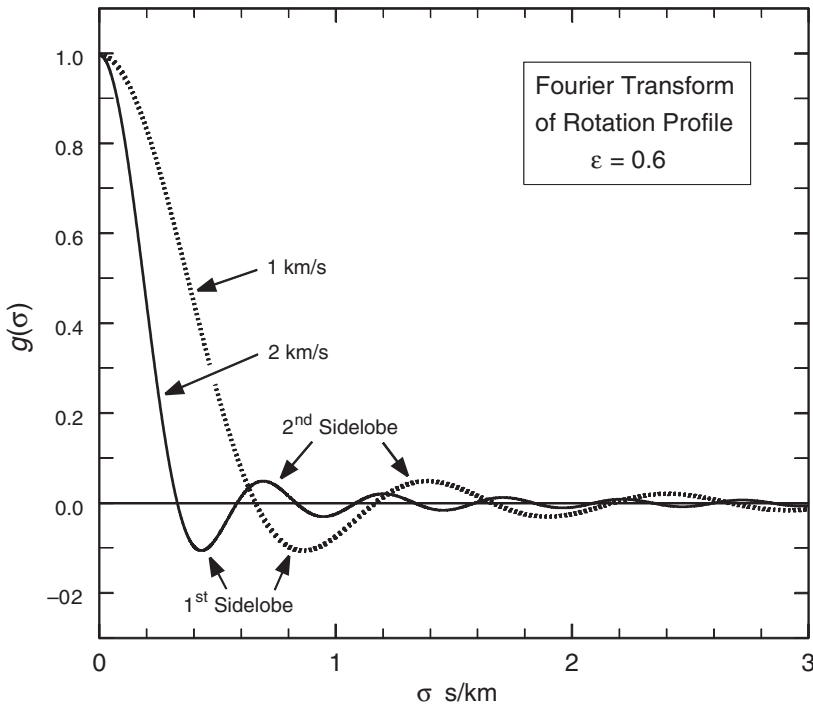
Fig. 18.11. The Fourier transform of the rotation profile is shown for $v\sin i = 1$ and 2 km/s. The abscissa scales inversely as with $v\sin i$. The sidelobes alternate sign and gradually diminish in amplitude.

$v\sin i$. Normally, log–log scales are used, as in Fig. 18.12. (We plot the *absolute value* of the amplitudes in order to use a logarithmic ordinate with negative sidelobes.) The logarithmic scale magnifies the sidelobes, where much of the important information is contained, and the $v\sin i$-scaling is changed into a simple translation in abscissa. Notice in Fig. 18.12 that the two curves are identical except for translation. In fact, we often compare a plot of $g(\sigma)$ for $v\sin i = 1$ km/s with the transforms of stellar line profiles; the log σ-scale difference between them gives $v\sin i$ directly.

When the rotational broadening is large compared to all other broadening, i.e., thermal motions, micro- and macroturbulence, and instrumental, the profiles of the spectral lines will be dominated by the shape of $G(\Delta\lambda)$. In such cases, Eq. (18.12) holds, and by including the convolution with the instrumental profile, according to Eq. (12.2), we can write the observed data as

$$D(\Delta\lambda) = H(\Delta\lambda) * G(\Delta\lambda) * I(\Delta\lambda) \tag{18.15}$$
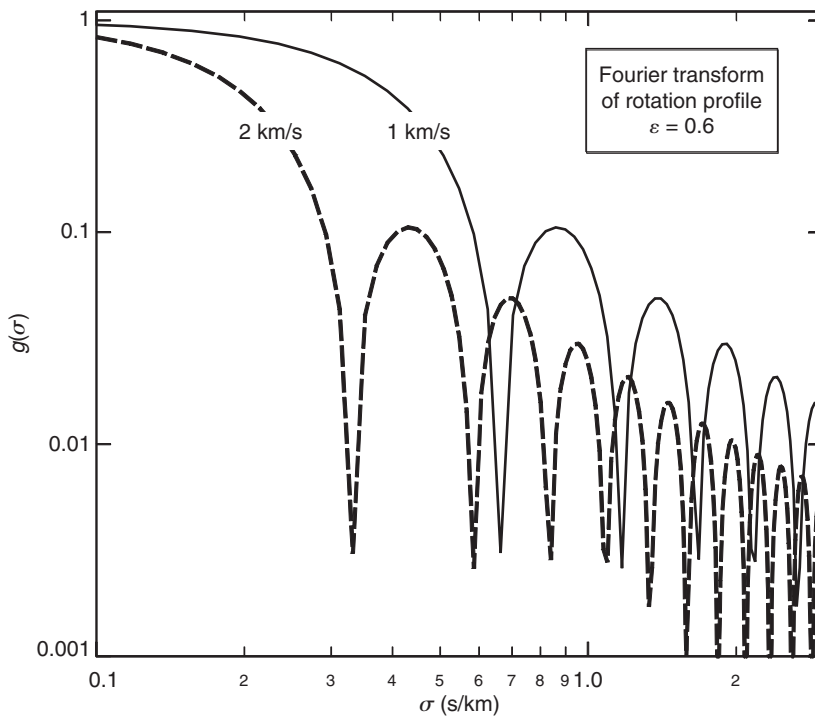
Fig. 18.12. A log–log plot of the transform of the rotation profiles shown in Fig. 18.11 is preferred because the shape is now identical except for a translation in σ coordinate and the important sidelobes are more prominently displayed.

or

$$d(\sigma) = h(\sigma)\, g(\sigma)\, i(\sigma). \tag{18.16}$$

The transforms can be compared directly, as illustrated in Fig. 18.13 with the Mg II $\lambda 4481$ line of α Peg. Naturally, it is the *line depth* for the star's spectral line, $D(\Delta\lambda) = 1 - F/F_c$, that is used and the continuum is the zero level. The effects of $h(\sigma)$ and $i(\sigma)$ are usually negligible because $v \sin i$ is so large and we are working at low Fourier frequencies where $h(\sigma)$ and $i(\sigma)$ are essentially constant.

Normal "white" noise is statistically at a constant level in the Fourier domain. The points on the right in Fig. 18.13, beyond $\sigma \approx 0.02\,\mathrm{s/km}$, are noise and indicate the noise level associated with these measurements. Signal concentrated into lobes rises higher above the noise, making the shape of the rotation transform easier to identify and measure compared to direct profile fitting, where the noise is uniformly distributed. Any additional line broadening will
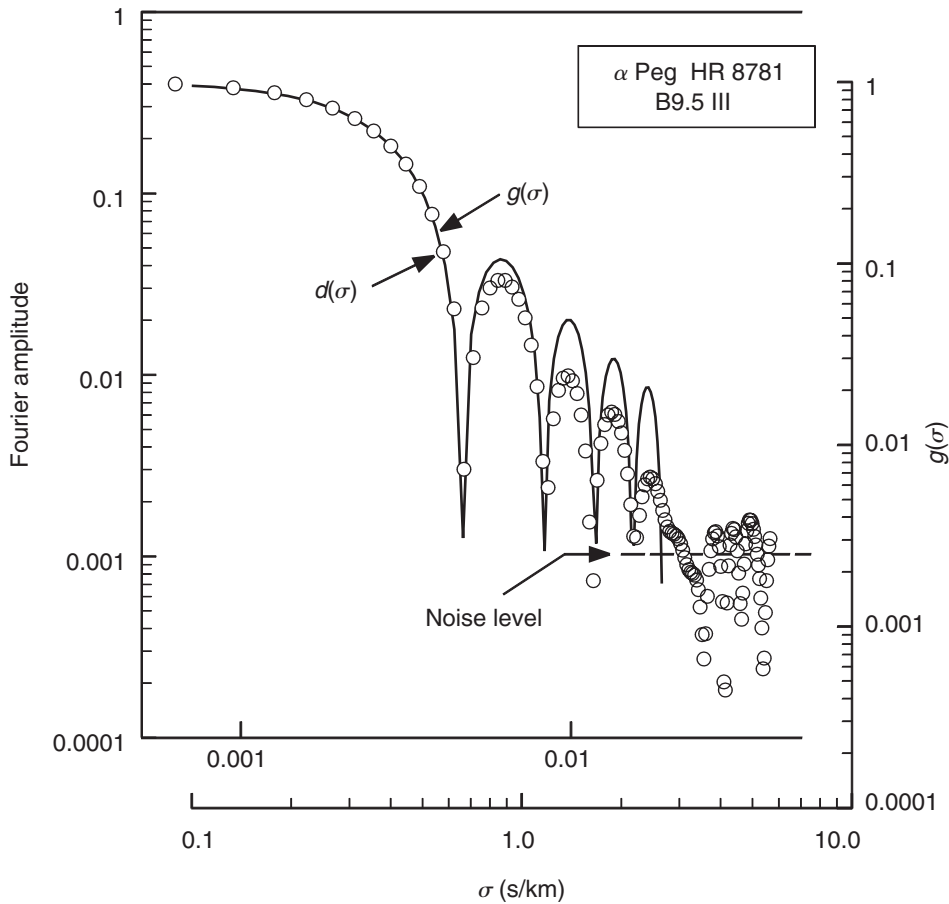
Fig. 18.13.   The data for λ4481 of α Peg (circles) are compared with the rotation profile (line) in the Fourier domain, where the rotation profile is computed for $v\sin i = 1$ km/s. Vertical translation of the two graphs matches the strength of the observed line, $d(\sigma)$ at $\sigma = 0$. Horizontal translation matches $g(\sigma)$ to $d(\sigma)$, with the difference in scales giving the rotation rate of 140 km/s. The increasing difference in amplitude between $g(\sigma)$ and $d(\sigma)$ arises from the filtering of the instrumental profile, the thermal profile, and macroturbulence. These need not be evaluated in order to determine $v\sin i$. Data from the Elginfield Observatory.

reduce the Fourier amplitudes and drive them toward the noise level, those at higher frequencies being reduced most.

Although the noise in the σ domain is proportional to the noise in the λ domain, according to Eq. (2.42), the amount of noise included increases with the wavelength interval. Specifically, the number of continuum points adjacent to the line itself should be kept to a minimum.

Transform width as a measure of $v \sin i$

Just as the profile width in larger $v \sin i$ situations is a respectable tool for finding $v \sin i$, the width of the transform can be used. One of the simplest ways to define the width of a transform is with the position of the first zero. This simple concept stems back to the early 1900s, well before observers had the necessary signal-to-noise ratios to make it work. For example, Carroll (1933a, b) derived an analytical form for the transform of $G(\lambda)$ with $\varepsilon = 0.6$,

$$g(\sigma) = \frac{J_1(u\beta)}{u\beta} - \frac{3\cos u\beta}{2u^2\beta^2} + \frac{3\sin u\beta}{2u^3\beta^3}, \tag{18.17}$$

in which $u\beta = 2\pi\Delta\lambda_L\sigma$ and J_1 denotes the first-order Bessell function. In particular, the σ positions of the first three zeros are given by

$$\Delta\lambda_L\,\sigma_1 = 0.660$$
$$\Delta\lambda_L\,\sigma_2 = 1.162$$
$$\Delta\lambda_L\,\sigma_3 = 1.661. \tag{18.18}$$

The multiplication of $g(\sigma)$ by $h(\sigma)$ in Eq. (18.16), may *add* zeros, but will not change the position of the zeros. Furthermore, if the rotation is reasonably large, the first two or three zeros of $g(\sigma)$ may occur at σ values where there is some significant signal. (This is obviously necessary if the position of the first zero is to be determined.)

Although the early attempt of Carroll and Ingram (1933) was not very successful, the method has worked well enough with modern observations. For example, Royer *et al.* (2002a, b) use σ_1 to determine rotation velocities of hundreds of early-type stars. The position of the first zero, while simple and convenient, ignores the rest of the information contained in the transform and therefore suffers the same limitations as the line-width technique discussed above.

Fourier analysis for moderate to small rotation

When the rotational broadening does not exceed the other broadeners by a factor of 2 or more, it becomes necessary to model the observed line profile more completely. Due allowance has to be made for the specific-intensity profile, $H(\Delta\lambda)$, for the instrumental profile, $I(\Delta\lambda)$, and especially for the combined Doppler shifts of macroturbulence and rotation using Eq. (18.12). We assume the radial–tangential form of macroturbulence in the discussion here. Therefore, Eq. (18.15) becomes

$$D(\Delta\lambda) = H(\Delta\lambda) * M(\Delta\lambda) * I(\Delta\lambda) \tag{18.19}$$

in which $M(\Delta\lambda)$ comes from a disk integration and includes the broadening of both macroturbulence and rotation. The transform of the observations is written as

$$d(\sigma) = h(\sigma)\,m(\sigma)\,i(\sigma). \qquad (18.20)$$

There are two possible path for analysis. A "model" of $d(\sigma)$ can be constructed by multiplying these three transforms together. The thermal component, $h(\sigma)$, scales $m(\sigma)$ to the equivalent width of the observed line (the $\sigma = 0$ ordinate), and the product $h(\sigma)\,m(\sigma)\,i(\sigma)$ is compared directly with the transform of the observed profile. The alternative is to divide the transform of the observed profile, $d(\sigma)$, by $h(\sigma)\,i(\sigma)$ and compare the "residual" transform with a model $m(\sigma)$. In this case, division by $h(\sigma)$ normalizes the residual transform to unity at $\sigma = 0$, as illustrated in Fig. 18.14. If the latter path is chosen, be aware of the enhanced noise toward higher frequencies.

The *shape* of the transform generally and any sidelobes, are used to distinguish rotational broadening from macroturbulence broadening. Disk-integration models are shown in Fig. 18.15. Compare this to Fig. 17.8. The appropriate ratio of macroturbulence broadening to rotational broadening, $\zeta_{RT}/v\sin i$, is chosen using the shape of the residual transform, $m(\sigma) = d(\sigma)/[h(\sigma)i(\sigma)]$, to select a model from the grid. As increasing amounts of macroturbulence are added to the rotation, the rotation sidelobes decline in amplitude and the frequencies of the zeros diminish. When $v\sin i$ is less than about twice ζ_{RT}, the sidelobe structure alters dramatically, the first sidelobe is squeezed out and the second sidelobe grows slightly in amplitude while continuing to move toward lower frequencies. Some considerable caution is called for when interpreting the sidelobes is this kind of situation.

Although individual spectral lines can be analyzed and their results averaged, it is usually advantageous to combine residual transforms for many lines. Lines of similar strength and excitation potential will not differ greatly in their depth of formation and they will all experience the same macroturbulence and rotational broadening. An example is given in Fig. 18.16. The agreement or otherwise of residual transforms gives us some information about how good our observed profiles are and how well we have modeled the $H(\Delta\lambda)$ profiles. Their scatter tells us how precisely the mean fits into the grid of $m(\sigma)$ models.

The fractional uncertainty on $v\sin i$ rises rapidly as rotational broadening drops below ζ_{RT}. This is the standard problem of attempting to measure a lesser broadening in the face of a larger one. In real cases, one often encounters rotation of 0–5 km/s in cool stars with corresponding errors of 0.5–0.2 km/s. In principle, the errors can be reduced by including more lines and increasing the signal-to-noise ratio of the observations.
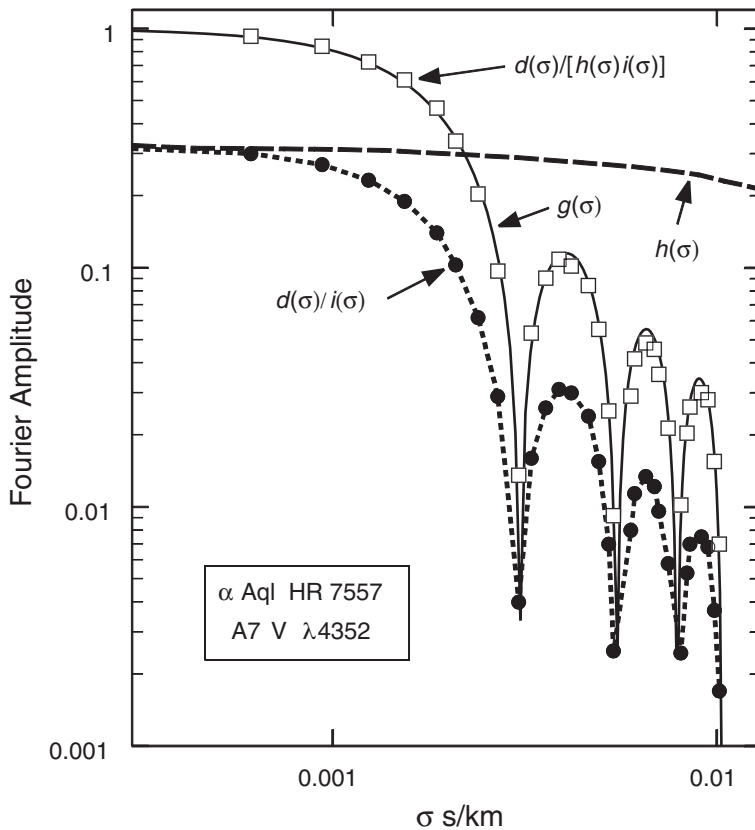
Fig. 18.14. Here the instrumental and thermal profiles are removed from the observations of the star to yield the residual transform shown by the squares. The residual is then compared to $g(\sigma)$ by horizontal translation to obtain $v \sin i = 209$ km/s. No macroturbulence has been included in the modeling. Data from the Elginfield Observatory.

Notice how much information is obtained for rotation studies from the higher Fourier frequencies. It is generally undesirable to choose a spectral resolving power no better than the anticipated value of $v \sin i$ unless you want the absolute minimum of information.

Additional aspects of spectroscopic rotation analysis

Limb Darkening: limb darkening acts like a weighting factor specifying how much of each Doppler shift enters the Doppler-shift distribution. When there is more darkening toward the limb, the largest Doppler shifts are weighted less, since they originate at the equatorial limb, and the broadening is less for a given rotation rate. Figure 18.17 illustrates the effect on the transforms. If one can
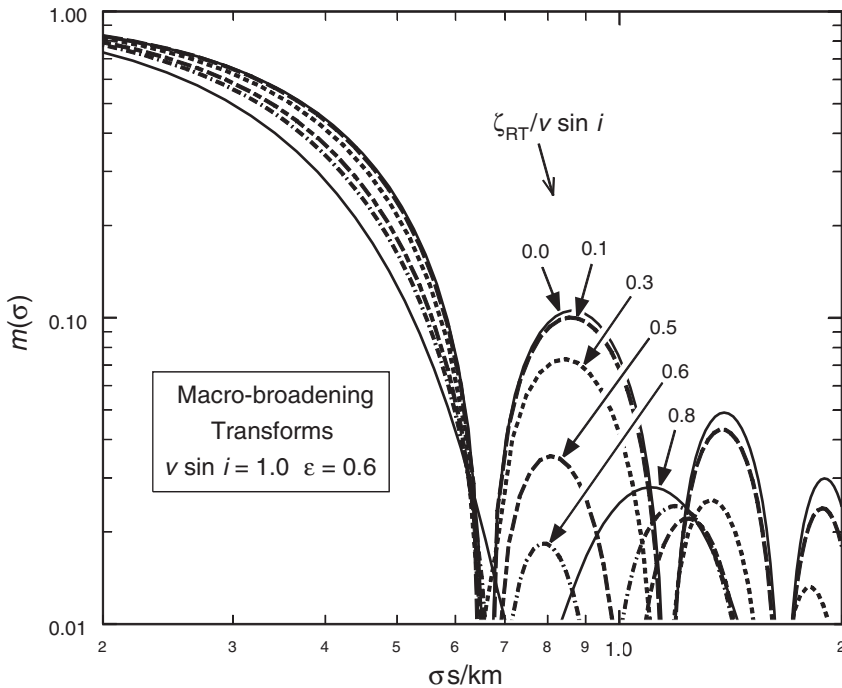
Fig. 18.15.   This is a grid of models giving $m(\sigma)$ for various values of $\zeta_{RT}/v\sin i$ as labeled. Small contributions of ζ_{RT} to the broadening simply reduces the amplitudes of the rotation sidelobes, but when ζ_{RT} exceeds about half the size of $v\sin i$, the nature of the sidelobe structure changes.

see the sidelobes with high enough signal-to-noise ratio, in principle it is possible to gain some information on the limb-darkening coefficient. If the signal-to-noise ratio is too low because other broadening agents enter and reduce the sidelobe heights, or if $v\sin i$ is simply too small, then one is forced to choose a value of ε in some other way such as Fig. 17.6. The sensitivity is such that over-estimating ε by $+0.1$ makes the deduced $v\sin i$ too high by $\approx 1.5\%$.

Differential rotation: differential surface rotation, meaning non-rigid rotation with the angular velocity depending on the latitude, is well documented on the Sun (e.g., Livingston 1969, Howard & Harvey 1970, Wilcox & Howard 1970, Brajša *et al*. 2002, Khutsishvili *et al*. 2002). Different tracers, however, show different rates of differential motion. Two sets of measurements are shown in Fig. 18.18; notice that the equator moves most rapidly. In the context of spectroscopic line broadening, it is the Doppler curve that is of direct interest. Differential rotation is often described by

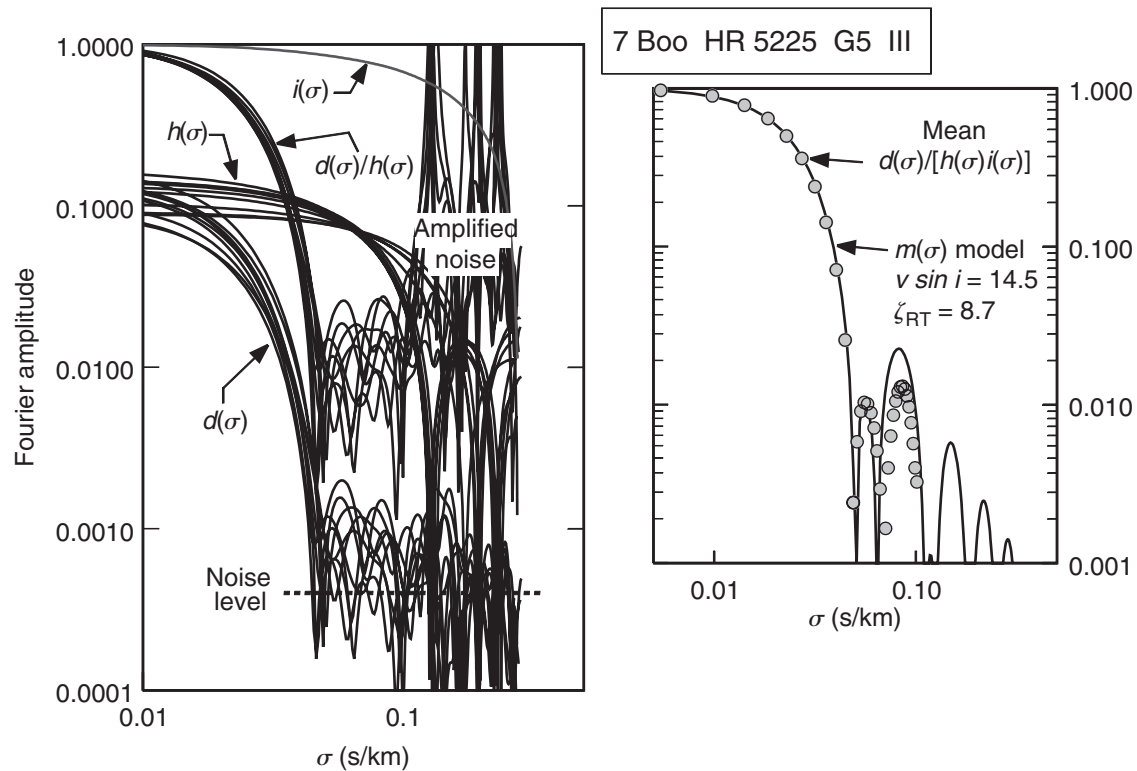$$v = v_0 + v_1 \sin^2\phi + v_2 \sin^4\phi. \tag{18.21}$$

Fig. 18.16. A Fourier analysis is illustrated using 7 Boo. On the left, the lower set of curves shows the transforms of the individual line profiles, $d(\sigma)$. After removal of the thermal profiles, $h(\sigma)$, one obtains the residual transforms shown in the top curves, labeled $d(\sigma)/h(\sigma)$. Notice the original noise level, determined by the signal-to-noise ratio in the observations, and the amplified noise in the σ regions where $h(\sigma)$ has small amplitudes. The filtering of the instrumental profile is shown as $i(\sigma)$. On the right, the circles show the mean residual transform with the instrumental profile removed. It is compared with a model, $m(\sigma)$, generated by disk integration. The agreement is very good except at higher frequencies where the amplified noise becomes significant.
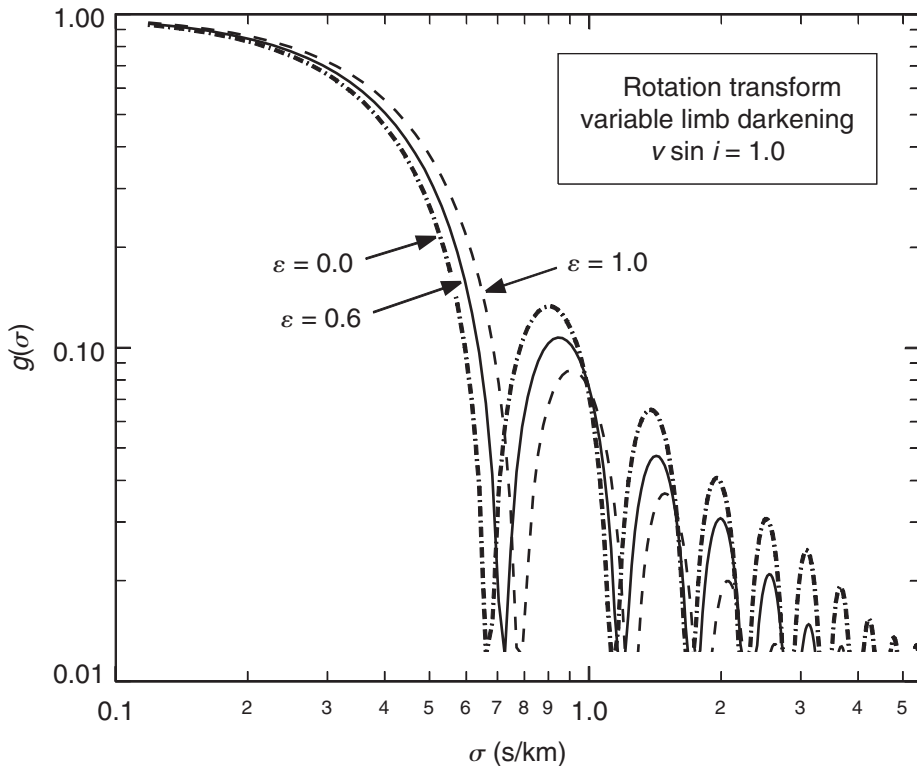
Fig. 18.17. Transforms of the rotation profile depends on the limb darkening coefficient ε. The uniform or undarkened case has $\varepsilon = 0$, while the "fully darkened" extreme has $\varepsilon = 1.0$. When the limb contributes less light, the Doppler shifts at the equatorial limb are weighted less, and the Doppler-shift distribution is narrower, resulting in a wider transform.

Here ϕ is the heliographic latitude and v_0 is the equatorial velocity. For the sidereal rate of the Sun, Eq. (18.21) is $v = 2.030 - 0.278 \sin^2 \phi - 0.278 \sin^4 \phi$, according to Scherrer *et al*. (1980). The values of these coefficients range considerably, with some observers placing v_0 as low as 1.93 km/s (see Schröter 1985). In some cases, the v_2 term is omitted (v_1 is then larger since it must express all of the latitude variation) and a dimensionless parameter expressing the relative strength of the differential effect is defined: $\alpha = -v_1/v_0$, which for the solar case is near 0.19.

The rotation profile becomes less "boxy" with increasing differential rotation because areas on the disk away from the equator contribute more weight to lower Doppler shifts in the Doppler-shift distribution. This alters the sidelobe strengths and widths, and in principle this can be used to detect the effect in stars (Gray 1977, 1982a, 1988, Bruning 1981, Dravins *et al*. 1990). Figure 18.19 shows
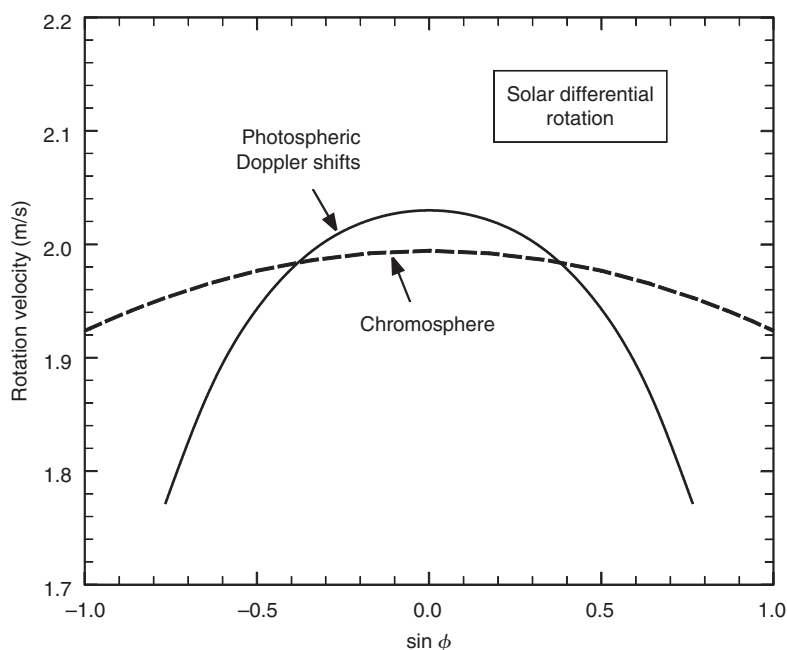
Fig. 18.18. The variation of the solar rotation rate with heliographic latitude amounts to ≈25% for the photosphere, but is much less for the chromosphere. Based on Scherrer *et al.* (1980) and Hoeksema and Scherrer (1987).

how $g(\sigma)$ depends on the amount of differential rotation; notably, the odd-number sidelobes decrease in amplitude while the even-number sidelobes remain relatively constant. Reversing the sign on v_1 enhances the odd-number sidelobes. A variation of the first-zero technique discussed above has been used with two zeros by Reiners and Schmitt (2003) to tackle the detection of differential rotation.

The effect of differential rotation on the Doppler-shift distribution also varies with the angle of inclination of the rotation axis because the surface projection factors for different latitudes change with inclination. When v_1 is negative, as in the solar case, the odd-number sidelobes have smaller amplitudes for smaller inclination angle, i.

The Gaussian error: when $v\sin i$ is comparable in size to ζ_{RT}, disk integrations show that the shape of $M(\Delta\lambda)$ is close to Gaussian. This fortuitous circumstance, combined in some cases with modest signal-to-noise ratios in the observations, has tempted some investigators to use the fictitious Gaussian model of macroturbulence (see Chapter 17) for the macro-broadening factor in their computed line profiles. In other cases this fictitious model has been convolved
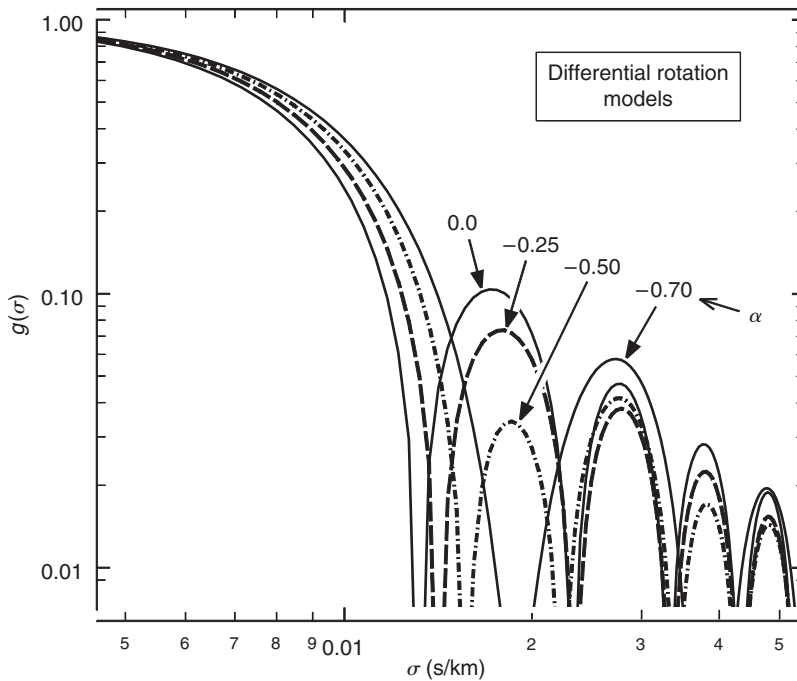
Fig. 18.19.   Increasing amounts of differential rotation reduces the size of the odd-numbered sidelobes. This is most easily seen by comparing the first to the second sidelobe. The latitude dependence of the rotation velocity in these models is specified by $v = v_0 + v_1 \sin^2 \phi$ and the important parameter is $\alpha = v_1/v_0$ as given in the figure. The abscissa scale is for $v_0 = 50$ km/s.

with the rotation profile $G(\Delta\lambda)$. One should be suspicious of any conclusions stemming from such an analysis.

Statistical corrections for axial projection

Evidence for random orientation of rotation axes is found in the lack of correlation between $v\sin i$ and galactic latitude or longitude, and in the frequency distribution of $v\sin i$ for homogeneous groups of stars (Struve 1945, Slettebak 1949, Huang & Struve 1954, 1960, Batten 1967, Abt 2001). Under the assumption of random orientation, it is possible to convert the average $v\sin i$ characterizing a group of stars to an average rotation velocity. Consider Fig. 18.20. Axes oriented at an angle i to the line of sight are represented by the shaded ring. The fraction of randomly oriented axes between i and $i + \mathrm{d}i$ is proportional to the solid angle subtended by the ring,

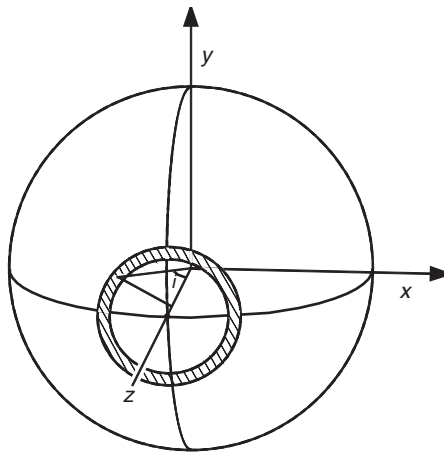$$P(i)\,\mathrm{d}i = 2\pi \sin i\,\mathrm{d}i.$$

Fig. 18.20. For randomly oriented rotation axes, the fraction at any angle of inclination *i* is proportional to the area of the shaded ring. We are much more likely to see a near-equator-on orientation than a near-pole-on orientation because the equator is a ring while the pole is a point.

The average $\sin i$ is then given by

$$\langle \sin i \rangle = \frac{\int P(i) \sin i \, \mathrm{d}i}{\int P(i) \, \mathrm{d}i} = \frac{\pi}{4}.$$

The integration need only be carried out over the hemisphere facing us, so *i* ranges from 0 to $\pi/2$.

This statistical result can be utilized to convert the average measured $v \sin i$ for a homogeneous group of stars, to an average rotational velocity using $\langle v \rangle = \langle v \sin i \rangle 4/\pi$. More complete discussions of statistics and velocity distributions are given in the literature (refer to Chandrasekhar & Münch 1950, Bernacca & Perinotto 1974, Gray 1988).

The axial orientation of individual stars is also of some interest for planetary searches (Doyle *et al*. 1984) and stellar magnetic activity (Gray 1989b). The Sun's rotation axis is inclined 7° to the ecliptic plane.

Rotational modulation

Just as Galileo could watch sunspots move across the disk of the Sun and determine the solar rotation period, so can we monitor modulation arising from rotation of stars more generally. The star need only have a non-uniform surface, invariant on a time scale that is long compared to the period of rotation. The physical source of the non-uniformity need not be understood physically. The signal itself can be photometric, such as a diminution in photometric flux

as a dark spot traverses the disk, or it can be spectroscopic, for example, a change in the emission strength of the Ca II H and K lines, or changes in the shape of line profiles. Stars seen close to pole-on show no rotational modulation, and stars without strong surface features are not going to show anything either. But when the period measurements are available they have the advantage of not being tied to a $\sin i$-projection factor the way the line broadening results are.

There are many techniques for period determination. One of the simplest is to minimize the scatter in a phase diagram. First, discern an approximate period by inspection of the data where the phase coverage is good. Second, construct a phase diagram by adding or subtracting multiples of the period from the times of observations to bring all the measurements onto a single cycle. Finally, adjust the period in small increments, reconstructing the phase diagram for each. (Digital computers are particularly happy doing these simple and boring calculations.) The period giving the cleanest phase diagram is adopted as the best choice (see Jurkevich 1971, Stellingwerf 1978, Marraco & Muzzio 1980, Cuypers 1986). One of the advantages of this scheme is that the periodic variation can have any shape and that shape will appear as a matter of course in the final phase diagram.

Fourier techniques, such as the periodograms discussed in Chapter 2, are often useful (see Gray & Desikachary 1973, Scargle 1982, Kurtz 1985), but should not be used without some study since the data-sampling window often produces confusing peaks in the transform. Furthermore, the signal itself is rarely a pure sinusoid, i.e., composed of a single frequency, so harmonics can be expected in the periodogram.

For truly long-lived features, the accuracy of the period can continue to increase as the number of cycles builds up with time, as discussed near the end of Chapter 2. A surface feature on ξ Boo A (G8 V), for example, was observed for many months, and allowed the 6.43 day period to be determined to $\approx \pm 0.01$ day (Toner and Gray 1988).

Rotational modulation of the H and K line emission has been extensively discussed (e.g., Horne & Baliunas 1986). Here the time scale of intrinsic variation is often only a few rotations. The period then becomes uncertain by a few per cent. One must also be on guard for multiple surface features that could fake a period of half or a third the true value. Differential rotation has also been measured using rotational modulation of the H and K emission (Gray & Baliunas 1997).

Simple photometric measurements are particularly effective for faint stars. Ground-based measurements can have errors as small as 1 mmag or 0.1%. Starspots as small as sunspots would therefore largely escape detection, but many stars have much larger spots, making photometric modulation a fairly common occurrence. Examples in the literature are numerous, for example, Stauffer (1984) and Frasca *et al*. (1998).

An extension of rotational modulation is rotational mapping of the stellar surface. This we briefly take up at the end of the chapter.

Rotation of dwarfs

The photospheric rotation of the Sun is rather small and varies with latitude, as noted above (Fig. 18.18). Although the sidereal equatorial rate is close to 2.0 km/s, the classical value, used in solar longitude specification is 1.92 km/s (25.38 day period, 2.865×10^{-6} rad/s angular velocity). This is the so-called Carrington rate, equal to the average rotation rate at a latitude of 16°. But the leisurely rotation of the Sun is not entirely typical of dwarfs.

The behavior of rotation along the main sequence is rather remarkable, as shown in Fig. 18.21. Early-type stars show a wide distribution of rotation rates, ranging from the typical resolution limit of $\approx$10 km/s up to hundreds of km/s.
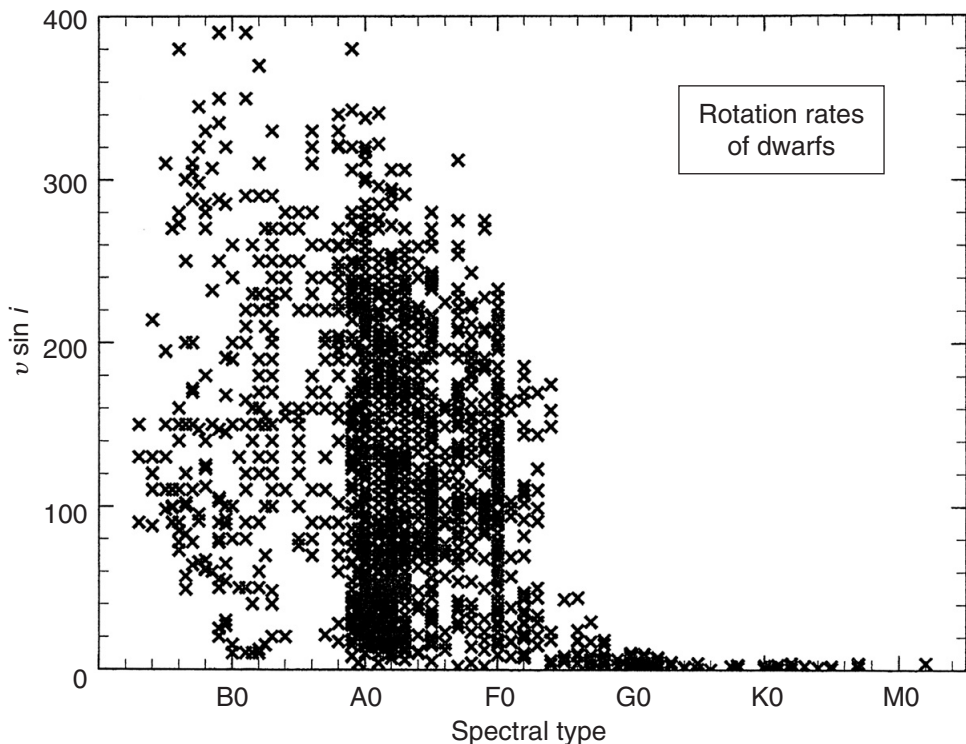

Fig. 18.21. Rapid rotation is normal for hot stars; slow rotation is seen for cool stars. The transition occurs near F5. Data from: Slettebak *et al.* (1975), Conti and Ebbets (1977), Soderblom (1982), Gray (1984b), Halbedel (1996), Penny (1996), Fekel (1997, 2003), and Royer *et al.* (2002b).
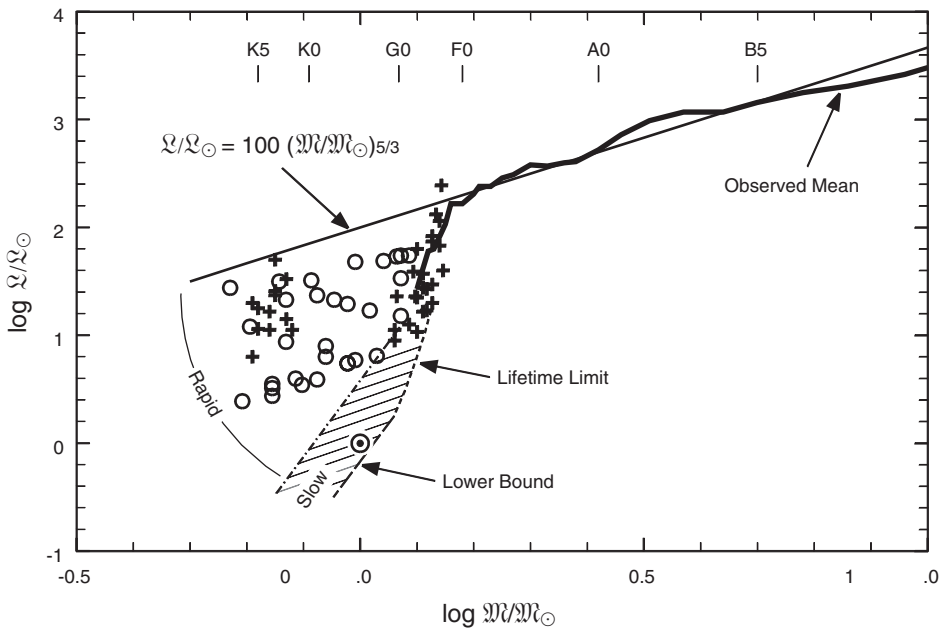
Fig. 18.22.   The surface rotation rates of dwarfs are used to compute the pseudo-angular momentum labeled "Observed mean." Most cool stars are found in the cross-hatched domain labeled "Slow," where they experience weak braking. Newly formed stars move rapidly downward from the straight line, across the region labeled "Rapid," and into the "Slow" domain. Cool Pleiades stars are denoted by the + symbols and cool stars in the α Per cluster by the circles.

The distribution within a narrow spectral band is a combination of true variation in rotation rates with the sin i projection factor. Through the F stars, we see a dramatic drop in rotation to only small values for the cool stars.

The F stars are the hottest stars where convective envelopes exist, and toward cooler stars, the convective envelopes encompass an increasingly greater fraction of the mass of the star. The indicators of magnetic activity, especially the enhancement of ultraviolet emission lines and the emission cores of the Ca II H and K lines, become increasingly strong over this very same interval. This can all be tied together with the hypothesis of a magnetic brake generated by interaction between the convective envelope and rotation in a process called a dynamo (discussed briefly below).

Stars come to the main sequence with a well-ordered rotation pattern. Consider the pseudo-angular momentum diagram (pseudo because we do not know the rotation profile inside the stars) shown in Fig. 18.22. Here

$$\mathscr{L} = \mathfrak{M} R \upsilon, \tag{18.22}$$

where $\mathfrak{M}$ is the mass of the star, R its radius, and v its (surface) equatorial rotation rate, is plotted as a function of mass. Mean rotation rates are shown for the hotter more massive stars. These data are reasonably represented by

$$\frac{\mathscr{L}}{\mathscr{L}_\odot} = 100 \left(\frac{\mathfrak{M}}{\mathfrak{M}_\odot} \right)^{5/3}. \tag{18.23}$$

It seems likely that this relation expresses the allotment of angular momentum per unit mass when stars are formed, including low-mass stars. But low-mass stars experience braking.

There seem to be two stages of rotational slow-down for cool dwarfs. Early in their life, as pre-main-sequence stars (T Tau stars) and new arrivals to the main sequence, they decelerate rapidly. This is seen most clearly with open clusters, where lower-mass stars in younger clusters are caught in the rapid-braking phase, showing rotation rates as high as 100 km/s. The evolutionary ages of these clusters point to a time scale of $\lesssim 30$ million years for the rapid-braking stage of G dwarfs, and perhaps one order longer for K dwarfs (van Leeuwnen & Alphenaar 1982, Soderblom *et al.* 1983, van Leeuwnen 1983, Stauffer 1984, Stauffer & Hartmann 1987, Stauffer *et al.* 1987). Some stars of the Pleiades and α Per clusters in the rapid-braking domain are shown by the symbols in Fig. 18.22. There are many papers on this topic including Dicke (1970), Vogel and Kuhi (1981), Smith *et al.* (1983), Bouvier *et al.* (1986), Kuwaler (1987), Stauffer *et al.* (1989), Jones *et al.* (1996), Rhode *et al.* (2001), Soderblom *et al.* (2001), Tinker *et al.* (2002), and Barnes (2003).

Once settled on the main sequence, cool stars enter a weak-braking phase with time scales of billions of years. The exact age dependence is disputed, but a rough value for solar-mass stars is given by

$$v \sin i \approx \frac{5}{\text{age}^{1/2}} \text{ km/s} \tag{18.24}$$

where "age" is in billions of years (Skumanich 1972, Soderblom 1983, Barry *et al.* 1987). The Sun, with a disk-integrated rate of 1.9 km/s, is well along in the weak-braking stage, rotating near the lower limit observed for G dwarfs.

Most dwarfs hotter than spectral type F seem to be content spinning rapidly for their entire main-sequence lifetime. Apparently they are not conducive to magnetic-braking phenomena. The exceptions to this general pattern are some peculiar A stars (Ap stars) and the metallic-line A stars (Am stars), which show anomalously slow rotation and evidence of rotational deceleration (Conti 1965, Abt 1979, Fleck 1980, Wolff 1981, Dravins *et al.* 1990). The distribution of rotation rates for A stars is not completely understood (Wolff *et al.* 1982),

but may reflect the distribution of angular momentum when these stars were formed.

Rotation of evolved stars

The changes in rotation as stellar radii grow and internal structure changes with evolution off the main sequence have been studied for many years (e.g., Huang & Struve 1953, Oke & Greenstein 1954, Herbig & Spalding 1955, Sandage 1955, Slettebak 1955, Abt 1957, 1958, Kraft 1968). The pattern of behavior has become clearer from studies using the advantages of modern equipment and Fourier analysis (Gray 1981, 1982c, 1988, 1989a, Gray & Nagar 1985, Gray & Toner 1986). Figures 18.23 and 18.24 show the observations for subgiants and giants. Putting together the declines seen in Figs. 18.21, 18.23, and 18.24, we can define a "rotation boundary" in the HR diagram. Refer back to Chapter 17, Fig. 17.18 to see the HR diagram with both the rotation and granulation boundaries. With few exceptions, stars on the hot side of the boundary rotate rapidly and those on the cool side slowly.

The majority of stars in the giant and subgiant region of the HR diagram evolved from the upper portion of the main sequence where rapid rotation occurs, so we can presume that most of them left the main sequence rotating rapidly. The evolutionary increase in moment of inertia adequately accounts for the drop in rotation from the main sequence to the F-star domain (Endal & Sofia 1979). Soon thereafter, as the surface temperature continues to drop, a sharp decline in rotation occurs that is unlikely to be the result of increased moment of inertia. A magnetic-dynamo brake is suspected, as discussed below.

Before crossing the rotation boundary, stars have a wide range of rotation, but after it, rotation is a single-valued function of spectral type given by

$$v = \frac{4}{\pi} \langle v \sin i \rangle = 15.6 - 4.2\,Sp \tag{18.25}$$

for class III giants, where the numerical spectral type Sp is 2.2 for G2, 2.3 for G3, . . . , 2.9 for G9, 3.0 for K0, etc. This is an observational result (Gray 1989a). At G2 III, the value is about 6.4 km/s, but slows to 2.2 km/s for K2 giants.

Supergiant stars show no sudden decrease in rotation. In the G- and K-star region, their rotation rates are ≲5–8 km/s, which is consistent with conservation of angular momentum and evolutionary changes in moment of inertia (Gray & Toner 1987). Such low rotation rates are probably too low to generate a magnetic brake (see the next section).
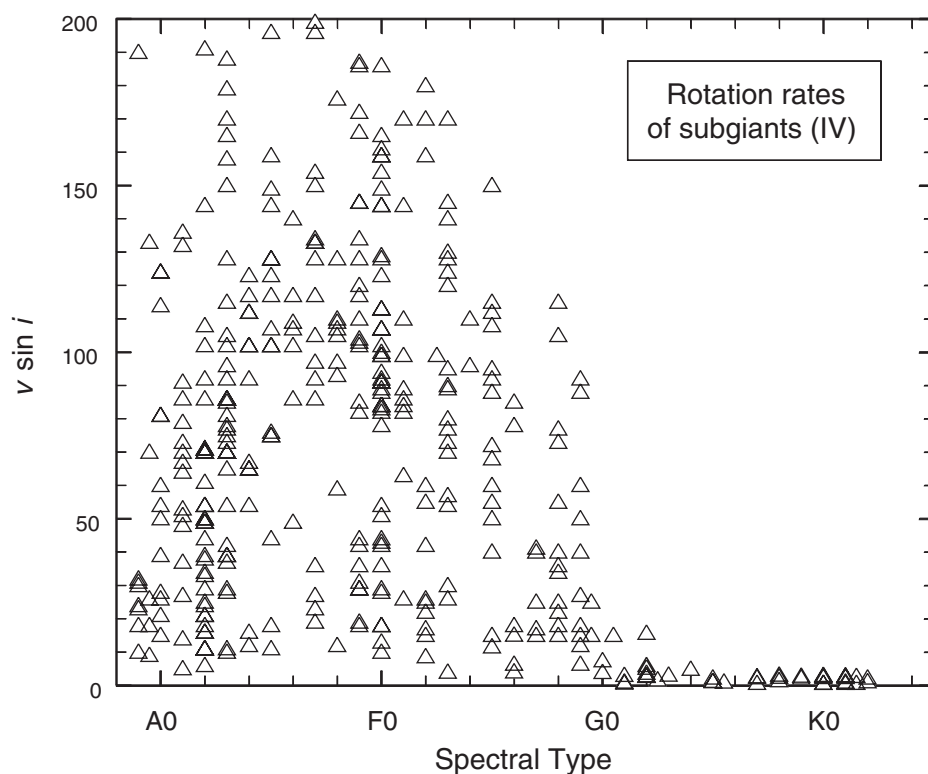
Fig. 18.23. Subgiants show a wide range of rotation rates for stars hotter than G0 IV, but slow rotation for cooler stars. Data from: Uesugi and Fukuda (1982), Gray and Nagar (1985), Fekel (1997, 2003), and Royer *et al*. (2002b).

Rotation of stars in the extreme upper right of the HR diagram has not been extensively studied because of the severe blending of lines and because the macroturbulence of these stars is rather large (e.g., Gray 2001). There is one direct measurement of the rotation of the M supergiant Betelgeuse by Uitenbroek *et al*. (1998) who found $v \sin i \approx 5$ km/s, which is not inconsistent with rough estimates of moment-of-inertia changes (Gray 2000). Stars returning across the HR diagram on evolutionary blue loops may have conserved enough angular momentum to spin up again. Sizable rotation is also seen for population II horizontal-branch stars (Peterson 1983, 1985a, b, Behr 2003).

One of the latest evolutionary stages we are able to measure is the white dwarf phase. Even though stars have shrunk to very small dimensions upon becoming white dwarfs, they rotate rather slowly. Typical $v \sin i$ values are ≈ 20 km/s, and none are seen rotating faster than ≈ 60 km/s (Greenstein *et al*. 1977, Pilachowski & Milkey 1987). Pulsars, with periods of ≈ 1 s, are thought to be rapidly rotating neutron stars, the core remnant of supernovae detonations.
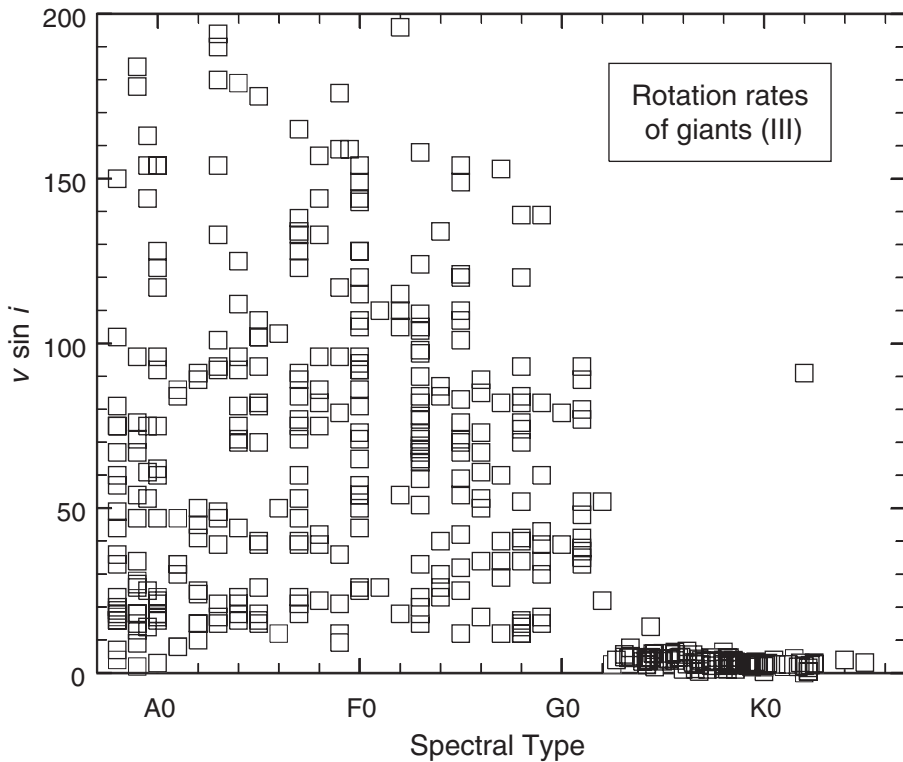
Fig. 18.24. Giants mimic the lower luminosity classes, but the drop in rotation occurs at G2 III. From G2 III to K2 III, rotation is a single-valued function of spectral type as given by Eq. (18.25). Data from: Alschuler (1975), Gray (1982c, 1989a), Hoffleit and Jaschek (1982), Royer *et al*. (2002b), and Fekel (2003).

Rotation and magnetic activity

Magnetic fields have not generally been found in hot stars. The peculiar A stars are the exception, and their fields are found to be strong and globally organized. As a result, a systematic variation of circular polarization occurs across the profiles of magnetically sensitive lines. Fields as small as 10 G (0.001T) can be detected, and fields up to several tens of thousands of gauss have been seen (Babcock 1962, Landstreet 1982, Stift 1986, Mathys 1988). As mentioned above, the Ap stars show evidence of rotational braking.

Direct measurement of the Zeeman effect for cool stars is more difficult because cool-star fields come in loops. The observer sees an approximately equal amount of field in opposite orientations, and there is little net polarization. The extra line broadening arising from the Zeeman splitting remains, but the field must exceed ≈0.5 kG to be detected (Robinson *et al*. 1980, Marcy

1984, Gray 1984a, Saar *et al*. 1986, Saar 1988, Gray 1988). At the same time, stellar magnetic activity is detected in enhanced coronal and chromospheric emission, including x-ray emission, UV emission lines, emission in the cores of the H and K lines, the filling in of the core of H_α and other strong lines, occasional flares, and starspots. From the solar example, these are known to be indirect indicators of magnetic fields. A great deal of evidence points toward the coupling of convection with rotation to generate the magnetic field, through one or several dynamo mechanisms. Durney and Latour (1978) employed the Rossby number as a simple dimensional statement that rotation can influence convection only if the convective motion is slow compared with the rotation. Using the period for the rotational time and t_{conv} for the time for convection to cycle or "turn over," the Rossby-number condition is

$$R_0 = P_{rot}/t_{conv} \lesssim 1 \qquad (18.26)$$

if a dynamo is to function. The theory of stellar convection is not well developed, but if the characteristic velocity is v_{conv}, and the characteristic length scale is ℓ, then since $P_{rot} = 2\pi R/v_{rot}$, we can write Eq. (18.26) as

$$R_0 = \frac{2\pi R}{v_{rot}} \frac{v_{conv}}{\ell} \lesssim 1,$$

or

$$v_{rot} \gtrsim 2\pi v_{conv}/(\ell/R). \qquad (18.27)$$

Since this is a rough dimensional argument, the factor of 2π is sometimes dropped. Rotation that is too low will not maintain the dynamo.

Several of the magnetic indicators and magnetic braking have been related to this dynamo criterion for stars on the cool side of the rotation boundary (for example, Gray 1981, 1989a, Catalano & Marilli 1983, Noyes *et al*. 1984, Soderblom 1985, Rucinski & VandenBerg 1986, among others). In effect, Eq. (18.27) says that although magnetic activity may indeed increase with rotation rate, it is really more correct to say it increases inversely with the Rossby number, and thereby properly include the convection factor. The truth of this statement is not universally accepted, e.g., Glebocki and Stawikowski (1988) argue that rotation alone gives a better interpretation of the data. Coronal x-rays in hotter stars, in contrast to cool stars, are apparently not connected to rotation (Wolff *et al*. 1986, Wolff & Heasley 1987).

The dynamo process generates magnetic fields, which in turn drive the diverse magnetic phenomena seen on cool stars. Spin-down of cool stars is one of them. The small amount of material that escapes in a stellar wind is ionized and so becomes entangled in the star's magnetic field until it is many

stellar radii from the star. By that time it has been "spun-up" to high angular velocities, and carries away with it much more angular momentum than it had at the stellar surface. This mechanism for dissipating angular momentum is called a magnetic brake (see Schatzman 1962, Weber & Davis 1967, Belcher & MacGregor 1976, Gray 1988).

Magnetic braking accounts for the rotation boundary in the HR diagram. Through Eq. (18.27), we can understand that convective envelopes are needed to engender dynamo action and the braking that comes with it. A natural explanation of the single-valued rotation rates for evolved stars expressed in Eq. (18.25) also follows: any rotation rate faster than given by Eq. (18.27) will produce braking, so virtually all stars evolving across the rotation boundary will experience braking and spin-down until their rotation is at the value where the dynamo can no longer be sustained. This is about 6.4 km/s at G2 III. The gradual decline in rotation toward later spectral types can also be understood with this general argument (Gray 1988, 1989a).

Although magnetic braking likely plays an important role in dissipating angular momentum for young stars approaching the main sequence, extended disks of material also seem to be an important mechanism for reducing angular momentum (e.g., Bouvier *et al.* 1997, Rebull *et al.* 2002).

Another important aspect of dynamo action is the magnetic cycle. Many dwarfs show cyclic changes corresponding to the ≈11 year solar magnetic cycle (Wilson 1968, 1978, Baliunas & Vaughan 1985).

Rapid rotators

The speediest rotators, if we exclude fossils such as neutron stars, are the emission-line B stars (Be stars). Some of them rotate at ≈450 km/s which is near their theoretical break-up velocity. The relations according to Slettebak (1966) are shown in Fig. 18.25 (see also Hardorp & Strittmatter 1968, Stoeckley 1968, Slettebak 1982). Mass is probably leaving these stars at their equators, and the resultant "disk" around the star gives the emission seen in the hydrogen lines. Numerous models have been proposed, e.g., McLaughlin (1961), Marlborough (1969), Limber (1970), and Poeckert and Marlborough (1978). A review of Be stars is given by Underhill and Doazan (1982).

Changes in stellar continua for stars rotating near their break-up rate have been computed by Sweet and Roy (1953), Collins (1966), and Faulkner *et al.* (1968). When a star rotates rapidly, it loses its spherical shape, and the effects of so-called gravity darkening become important (von Zeipel 1924, Eddington 1926, Tassoul 1978). Observational parameters such as $B - V$, M_V, and T_{eff} become functions of the aspect angle. Scatter in the zero-age main sequence
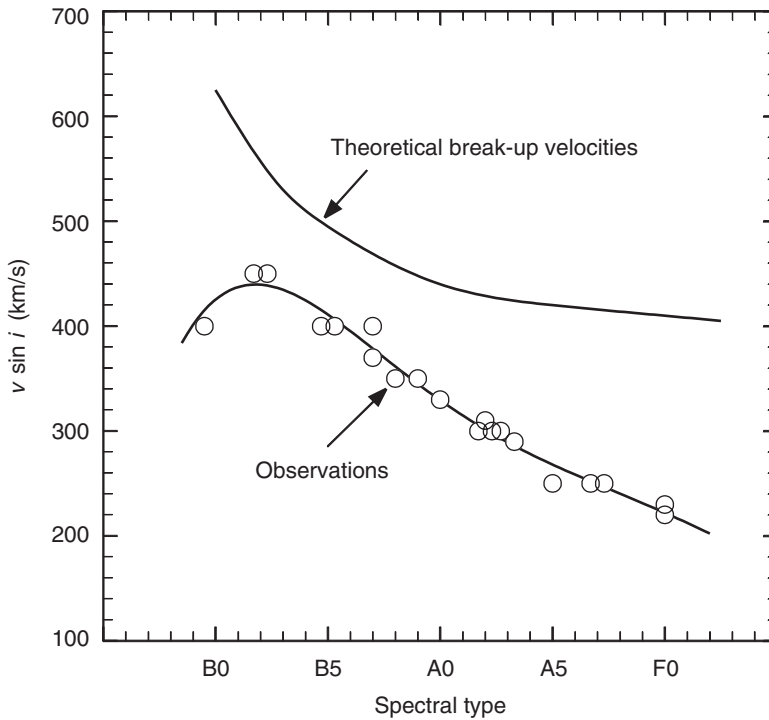
Fig. 18.25. The fastest rotation rates are shown by the symbols. The theoretical break-up velocities (top curve) approach the observed relation most closely in the B-star range, where many of the spectra show emission lines. Data from Slettebak (1966).

may in part be due to rotation, as discussed by Kraft and Wrubel (1965), Roxburgh and Strittmatter (1965, 1966a, b), Bless and Code (1972), Hauck and Slettebak (1989), and Mathew and Rajamohan (1992).

The effect of rapid rotation on equivalent widths of spectral lines was considered by Collins (1968), Hardorp and Strittmatter (1968), Stoeckley (1968), and Collins and Truax (1995). Changes in line strengths were found to be very small except for the extreme cases near break-up, but even then, Slettebak *et al.* (1980) conclude that spectral type is never altered by more than 1.5 subclasses, and it is doubtful that rapidly rotating stars can be classified with such precision. Stoeckley (1968) analyzed photoelectric data for five extreme rotators and showed how v can be separated from i. Very precise measurements are needed in order to do this type of work.

Occasionally one sees unusual line profiles caused by a combination of rapid rotation and the aspect of view. One such case is Vega (α Lyr, HR 7001, A0 V), our photometric standard of Chapter 10. The star has relatively
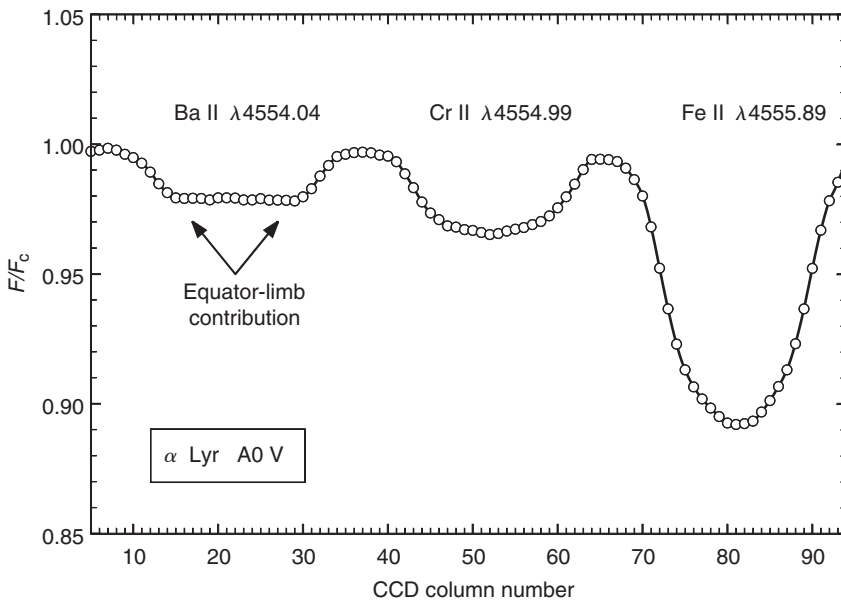
Fig. 18.26.   Vega (α Lyr) shows some profiles that are shaped by the non-uniform distribution of the specific-intensity profile across the disk. Rapid rotation combined with near pole-on view conspires to have the Doppler-shift distribution of $\lambda 4554.04$ dominated by contributions from the equatorial-limb areas (extremes of the profile) with much less than normal contribution from the central portions of the disk (center of the profile). Elginfield observatory data.

narrow lines with $v \sin i \approx 22$ km/s, but actually is a rapid rotator with $v \approx 245$ km/s seen nearly pole-on (Gulliver *et al.* 1994). With this aspect, the limb and equator are nearly the same. At the equator the centripetal force reduces the effective surface gravity enough to alter the ionization balance and strengthen the local I_ν profile of certain species. The Doppler-shift distribution for such species then arises largely from the two equatorial regions near the limb, i.e., it is bimodal. Figure 18.26 illustrates one of these "strange" profiles.

A few rapidly rotating single stars also appear on the cool side of the rotation boundary (FK Com stars, for instance). How they can have escaped the braking processes experienced by normal cool stars is a puzzle. Coalescence of binary components has been suggested (Bopp & Stencel 1981, Walter & Basri 1982, McCarthy & Ramsey 1984, Baliunas & Guinan 1985, Fekel *et al.* 1986, Huovelin *et al.* 1987). Perhaps they are young stars on their way to the main sequence (Carrasco *et al.* 1980, Bopp *et al.* 1981, Vogt 1983, Vilhu *et al.* 1987; see also Drake *et al.* 2002).
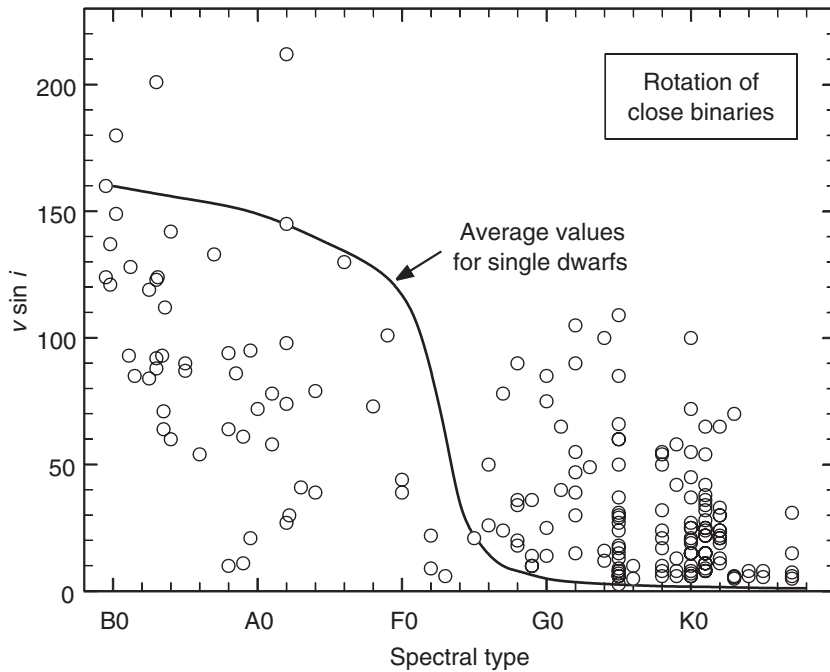
Fig. 18.27. Interacting binaries exchange orbital and rotational angular momentum through tidal coupling. Hot binaries are slowed down by this process and rotate more slowly than single stars, while cool binaries are sped up and rotate more rapidly than their single counterparts.

Rotation of binary stars

Widely separated binaries behave much like single stars since the tidal forces are small (Slettebak 1963, Weiss 1974). Close binaries, however, always show altered rotation. Figure 18.27 shows that on the average close binaries of early spectral type rotate slower than single stars, while those of later type often rotate many times faster than their single counterparts. The tidal coupling between the components in a binary makes the rotational period of the stars follow their orbital period. The simplest case occurs for orbits of low eccentricity. Then tidal coupling makes the two periods equal and there is exact synchronization.

The life of a binary becomes more complicated when the orbit is eccentric. The tidal forces, being differential gravitational forces, vary as the inverse cube of the distance. Consequently, coupling forces at periastron dominate, and the rotation rate tries to match the orbital angular velocity near periastron, which is higher than at other orbital positions (Kepler's second law). The resulting rotational period is therefore shorter than the orbital period.

The degree of tidal interaction depends on the size of the orbit compared to the size of the stars, expressed as the semi-major axis over the stellar radius a/R, and it takes time for the angular-momentum transfer to occur. An example worked out by Tassoul (1987) indicates a synchronization time comparable to the main sequence lifetime for a $9\,M_\odot$ star ($\approx 2 \times 10^7\,\mathrm{yr}$) when the semi-major axis is ≈ 20 times larger than the stellar radius. Consequently, one expects altered rotation for binaries having orbits smaller than this, unless they are very new arrivals on the main sequence. The tidal interaction depends only weakly on mass whereas the main sequence lifetime depends strongly on mass. Synchronization effects are therefore more complete for lower-mass stars. Observational statistics are given by Levato (1976), Giuricin *et al.* (1984a, c), Abt and Levy (1985), and Hall (1986), for example.

Time considerations become even more relevant for post-main sequence binaries, where the stellar radii change on much shorter time scales. Stars more luminous than class II–III giants exist for times too short to respond to tidal control, unless a/R approaches unity.

On the cool side of the rotation boundary, tidal coupling feeds orbital angular momentum into the individual stars, overpowering the braking mechanisms that are so effective in slowing rotation of single stars. A comparison of rotation characteristics with coupling theory is given by Hall (1990). The results of the "extra" rotation are strikingly seen in the G and K stars of luminosity classes III and IV, where their magnetic activity is greatly enhanced compared to single stars. Most notably, their chromospheric emission lines are very strong and they produce giant dark starspots (see Huisong & Xuefu 1987, Strassmeier *et al.* 1988, 1990 for more details).

Tidal forces also circularize binary orbits, but the time scale is longer and the distance range smaller than for synchronization effects (Giuricin *et al.* 1984a–c, Tassoul 1988).

Contact binaries are considerably more complicated (Plavec 1986), and because of the mass exchange across the Roche lobe, sporadic variations in the rotation may even occur (e.g., Olson 1984). The rotation profile essentially shows the shape of the two stars, another example of the rotational Doppler-shift distribution (Shajn & Struve 1929, Anderson & Shu 1979, Anderson *et al.* 1983).

Rotational mapping

Rotational mapping is also called Doppler imaging. In Fig. 18.28 we review the one-to-one correspondence between position within the Doppler-shift distribution and longitude on the star for an equator-on aspect of view. Surface features that alter the amount of light coming from restricted
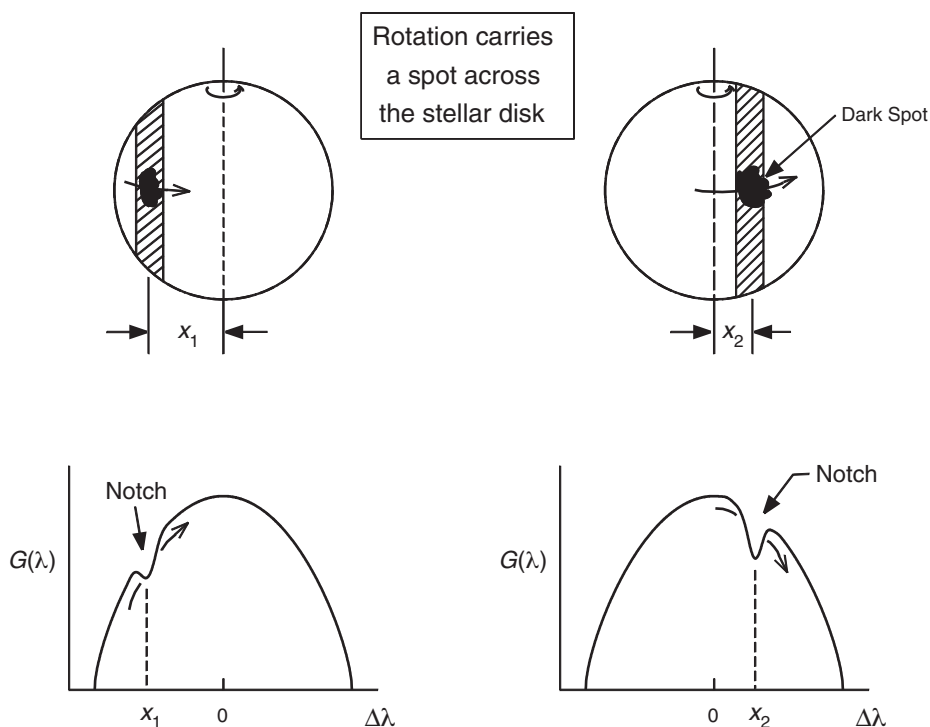
Fig. 18.28. The position in the Doppler-shift distribution corresponding to the spot has less light, producing a notch or dip. As rotation carries the spot across the stellar disk, the position of the notch moves across the Doppler-shift distribution and its strength changes with the projected area of the spot.

longitude bands will introduce structure into the rotation profile. In the simplest case, a dark spot reduces the contribution to the light in one of the strips, as illustrated in Fig. 18.28. This produces a dip or notch in the rotation function $G(\Delta\lambda)$ at the Doppler shift corresponding to that strip. When $G(\Delta\lambda)$ shapes absorption lines, it is seen upside down and the notch looks like an emission bump in the profile. The bump appears on the short-wavelength side of the profile as the spot becomes visible on the approaching limb. It migrates across the profile, growing stronger as the spot becomes more nearly face-on, reaching its largest size as the spot crosses the star's meridian. As the bump continues on the receding side of the disk, the same pattern is played in reverse, the bump fading in size and moving to its maximum positive Doppler shift. More generally, the Doppler shift for a spot of latitude ℓ and longitude L is given by

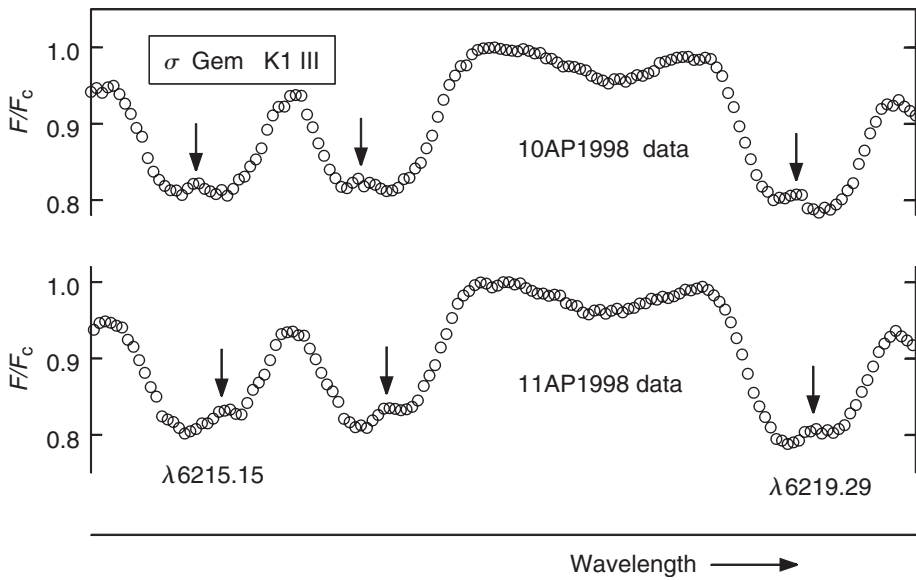$$\Delta\lambda = v \sin i \cos \ell \sin L \, \text{km/s}. \tag{18.28}$$

Fig. 18.29.   The K giant, σ Gem, has large spots. In these exposures, taken on consecutive nights, the bumps have progressed across the profiles. Data from the Elginfield Observatory.

The higher the spot latitude, the more restricted is the $\Delta\lambda$ range around the line center. When the rotation axis is not perpendicular to the line of sight, latitude information is also contained in the fraction of the rotation cycle over which the spot or bump is visible. If the latitude is high and the inclination of the rotation axis is small (pole toward us), the spot may be visible continuously. As the bump moves back and forth through the profile, its size will change with the projected area of the spot.

Such considerations assume a single time-stable position-stable spot. Furthermore, spots as small as those seen on the Sun would be very hard to detect in stellar line profiles; they simply cover too little of the solar disk. A bump like the one shown in Fig. 18.29 corresponds to a rather large spot by solar standards, but many stars show large spots. The spot bumps were first recognized in HR 1099 by Fekel (1983).

The decoding of profile variations into surface maps has some ambiguity, but nevertheless has been developed into a useful research tool (Goncharsky *et al.* 1982, Vogt & Penrod 1983, Vogt *et al.* 1987, Rice *et al.* 1989, Strassmeier & Rice 1998, Stout-Batalha & Vogt 1999, among many others). Differential rotation has even been mapped (e.g., Barnes *et al.* 2000, Collier Cameron 2002).

In addition to starspots, rotational mapping of chemical areas occurring on Ap stars and their relatives has become common, for example, Khokhlova *et al.*

(1986) and Rice and Wehlau (1990, 1994). When $v \sin i$ is less than about 10 km/s, the spatial resolution is lost, but variations in line broadening can still yield interesting information concerning areas having enhanced velocity fields (Toner & Gray 1988) or magnetic fields (Kochukhov *et al*. 2004).

References

Abt, H. A. 1957. *Ap. J.* **126**, 503.
  1958. *Ap. J.* **127**, 658.
  1979. *Ap. J.* **230**, 485.
  2001. *Ast. J.* **122**, 2008.
Abt, H. A. & S. G. Levy 1985. *Ap. J. Suppl.* **59**, 229.
Abt, H. A. & N. I. Morrell 1995. *Ap. J. Suppl.* **99**, 135.
Abt, H. A., H. Levato, & M. Grosso 2002. *Ap. J.* **573**, 359.
Alschuler, W. R. 1975. *Ap. J.* **195**, 649.
Anderson, L. & F. H. Shu 1979. *Ap. J. Suppl.* **40**, 667.
Anderson, L., D. Stanford, & D. Leininger 1983. *Ap. J.* **270**, 200.
Babcock, H. W. 1962. *Astronomical Techniques*, ed. W. A. Hiltner. (Chicago: Univ Chicago), p. 107.
Baliunas, S. L. & E. F. Guinan 1985. *Ap. J.* **294**, 207.
Baliunas, S. L. & A. H. Vaughan 1985. *Ann. Rev. Ast. Ap.* **23**, 379.
Barnes, J. R., A. Collier Cameron, D. J. James, & J.-F. Donati 2000. *Mon. Not. Roy. Ast. Soc.* **314**, 162.
Barnes, S. A. 2003. *Ap. J.* **586**, 464.
Barry, D. C., R. H. Cromwell, & E. K. Hege 1987. *Ap. J.* **315**, 264.
Batten, A. H. 1967. *On the Evolution of Double Stars*, ed. J. Dommenget, *Comm. Obs. Roy. Belgique*, Ser. B, p. 68.
Behr, B. B. 2003. *Ap. J. Suppl.* **149**, 67.
Belcher, J. W. & K. B. MacGregor 1976. *Ap. J.* **210**, 498.
Bernacca, P. L. & M. Perinotto 1970–71. *Contributi dell'Osservatorio Astrofisico dell'Universita di Padova in Asiago*, Nos. 239 and 250.
  1974. *Ast. Ap.* **33**, 443.
Bless, R. C. & A. D. Code 1972. *Ann. Rev. Ast. Ap.* **10**, 197.
Bopp, B. W. & R. E. Stencel 1981. *Ap. J. Lett.* **247**, L131.
Bopp, B. W., P. V. Noah, A. Klimke, & J. Africano 1981. *Ap. J.* **249**, 210.
Bouvier, J., C. Bertout, W. Benz, & M. Mayor 1986. *Ast. Ap.* **165**, 110.
Bouvier, J., M. Forestini, & S. Allain 1997. *Ast. Ap.* **326**, 1023.
Boyarchuk, A. A. & I. M. Kopylov 1964. *Crimean Ap. Obs. Pub.* **31**, 44.
Brajša, R., H. Wöhl, B. Vršnak, V. Ruždjak, F. Clette, & J.-F. Hichedez 2002. *Ast. Ap.* **392**, 329.
Bruning, D. H. 1981. *Ap. J.* **248**, 274.
Carrasco, L., J. Franco, & M. Roth 1980. *Ast. Ap.* **86**, 217.
Carroll, J. A. 1933a. *Mon. Not. Roy. Ast. Soc.* **93**, 478.
  1933b. *Mon. Not. Roy. Ast. Soc.* **93**, 680.
Carroll, J. A. & L. J. Ingram 1933. *Mon. Not. Roy. Ast. Soc.* **93**, 508.
Catalano, S. & E. Marilli 1983. *Ast. Ap.* **121**, 190.
Catalano, S. & J. R. Stauffer, eds. 1991. *Angular Momentum Evolution of Young Stars*. (Dordrecht: Kluwer).

Chandrasekhar, S. & G. Münch 1950. *Ap. J.* **111**, 142.
Chauville, J., J. Zorec, D. Ballereau, N. Morrell, L. Cidale, & A. Garcia 2001. *Ast. Ap.* **378**, 861.
Collier Cameron, A. 2002. *Ast. Nach.* **323**, 336.
Collins, G. W., II 1966. *Ap. J.* **146**, 914.
    1968. *Ap. J.* **152**, 847.
Collins, G. W., II & R. J. Truax 1995. *Ap. J.* **439**, 860.
Conti, P. S. 1965. *Ap. J.* **142**, 1594.
Conti, P. S. & D. Ebbets 1997. *Ap. J.* **213**, 438.
Cuypers, J. 1986. *Ast. Ap.* **167**, 282.
De Medeiros, J. R. & M. Mayor 1999. *Ast. Ap. Suppl.* **139**, 433.
Dicke, R. H. 1970. *Stellar Rotation*, ed. A. Slettebak. (Dordrecht: Reidel), p. 289.
Doyle, L. R., T. J. Wilcox, & J. J. Lorre 1984. *Ap. J.* **287**, 307.
Drake, N. A., R. de la Reza, L. da Silva, & D. L. Lambert 2002. *Ast. J.* **123**, 2703.
Dravins, D., L.Lindegren, & U. Torkelsson 1990. *Ast. Ap.* **237**, 137.
Durney, B. R. & J. Latour 1978. *Geophys. Ap. Fluid Dyn.* **9**, 241.
Eddington, A. S. 1926. *The Internal Constitution of the Stars*. (New York: Dover), p. 282.
Elvey, C. T. 1929. *Ap. J.* **70**, 141.
Endal, A. S. & S. Sofia 1979. *Ap. J.* **232**, 531.
Faulkner, J., I. W. Roxburgh, & P. A. Strittmatter 1968. *Ap. J.* **151**, 203.
Fekel, F. C., Jr. 1983. *Ap. J.* **268**, 274.
    1997. *Pub. Ast. Soc. Pacific* **109**, 514.
    2003. *Pub. Ast. Soc. Pacific* **115**, 807.
Fekel, F. C., T. J. Moffett, & G. W. Henry 1986. *Ap. J. Suppl.* **60**, 551.
Fleck, R. C., Jr. 1980. *Ap. J.* **240**, 218.
Frasca, A., E. Marilli, & S. Catalano 1998. *Ast. Ap.* **333**, 205.
Giuricin, G., F. Mardirossian, & M. Mezzetti 1984a. *Ast. Ap.* **131**, 152.
    1984b. *Ast. Ap.* **134**, 365.
    1984c. *Ast. Ap.* **135**, 393.
Glebocki, R. & A. Stawikowski 1988. *Ast. Ap.* **189**, 199.
Goncharsky, A. V., V. V. Stepanov, V. L. Khokhlova, & A. G. Yagola 1982. *Sov. Ast.* **26**, 690.
Gray, D. F. 1977. *Ap. J.* **211**, 198.
    1981. *Ap. J.* **251**, 155.
    1982a. *Ap. J.* **258**, 201.
    1982b. *Ap. J.* **261**, 259.
    1982c. *Ap. J.* **262**, 682.
    1984a. *Ap. J.* **277**, 640.
    1984b. *Ap. J.* **281**, 719.
    1988. *Lectures on Spectral-Line Analysis: F, G, and K Stars*. (Arva, Ontario: The Publisher), Chapter 5.
    1989a. *Ap. J.* **347**, 1021.
    1989b. *Pub. Ast. Soc. Pacific* **101**, 1126.
    2000. *Ap. J.* **532**, 487.
    2001. *Pub. Ast. Soc. Pacific* **113**, 1378.
Gray, D. F. & S. L. Baliunas 1997. *Ap. J.* **475**, 303.
Gray, D. F. & K. Desikachary 1973. *Ap. J.* **181**, 523.
Gray, D. F. & P. Nagar 1985. *Ap. J.* **298**, 756.
Gray, D. F. & C. G. Toner 1986. *Ap. J.* **310**, 277.
    1987. *Ap. J.* **322**, 360.

Greenstein, J. L., A. Boksenberg, R. Carswell, & K. Shortridge 1977. *Ap. J.* **212**, 186.

Gulliver, A. F., G. Hill, & S. J. Adelman 1994. *Ap. J. Lett.* **429**, L81.

Halbedel, E. M. 1996. *Pub. Ast. Soc. Pacific* **108**, 833.

Hall, D. S. 1986. *Ap. J. Lett.* **309**, L83.

    1990. *Active Close Binaries*, ed. C. Ibanoglu. (Dordrecht: Kluwer), p. 95.

Hardorp, J. & P. A. Strittmatter 1968. *Ap. J.* **153**, 465.

Hauck, B. & A. Slettebak 1989. *Ast. Ap.* **214**, 153.

Herbig, G. H. & J. F. Spalding, Jr. 1955. *Ap. J.* **121**, 118.

Hill, G. M. 1995. *Ast. Ap.* **294**, 536.

Hoeksema, J. T. & P. H. Scherrer 1987. *Ap. J.* **318**, 428.

Hoffleit, D. & C. Jaschek 1982. *The Bright Star Catalogue*, 4th edn. (New Haven: Yale Univ. Obs.).

Horne, J. H. & S. L. Baliunas 1986. *Ap. J.* **302**, 757.

Howard, R. 1984. *Ann. Rev. Ast. Ap.* **22**, 131.

Howard, R. & J. Harvey 1970. *Solar Phys.* **12**, 23.

Huang, S.-S. & O. Struve 1953. *Ap. J.* **118**, 463.

    1954. *Ann. d'Ap.* **17**, 85.

    1960. *Stellar Atmospheres*, ed. J. L. Greenstein. (Chicago: Univ. Chicago), p. 321.

Huisong, T. & L. Xuefu 1987. *Ast. Ap.* **172**, 74.

Huovelin, J., V. Piirola, O. Vilhu, Y. S. Efimov, & N. M. Shakhovskoy 1987. *Ast. Ap.* **176**, 83.

Johns-Krull, C. M. 1996. *Ast. Ap.* **306**, 803.

Jones, B. F., D. A. Fischer, & J. R. Stauffer 1996. *Ast. J.* **112**, 1562.

Jurkevich, I. 1971. *Ap. Space Sci.* **13**, 154.

Khokhlova, V. L., J. B. Rice, & W. H. Wehlau 1986. *Ap. J.* **307**, 768.

Khutsishvili, E. V., M. Sh. Gigolashvili, & T. M. Kvernadze 2002. *Solar Phys.* **206**, 219.

Kochukhov, O., S. Bagnulo, G. A. Wade, *et al.* 2004. *Ast. Ap.* **414**, 613.

Kraft, R. P. 1968. *Stellar Astronomy*, Vol. 1, ed. H.-Y. Chiu, R. L. Warasila, & J. L. Remo. (New York: Gordon & Breach), p. 317.

    1970, *Spectroscopic Astrophysics*, ed. G. H. Herbig. (Berkeley: Univ. California Press), p. 385.

Kraft, R. P. & M. H. Wrubel 1965. *Ap. J.* **142**, 703.

Kurtz, D. W. 1985. *Mon. Not. Roy. Ast. Soc.* **213**, 773.

Kuwaler, S. D. 1987. *Pub. Ast. Soc. Pacific* **99**, 1322.

Landstreet, J. D. 1982. *Ap. J.* **258**, 639.

Levato, H. 1976. *Ap. J.* **203**, 680.

Limber, D. N. 1970. *Stellar Rotation*, IAU Coll., ed. A. Slettebak. (New York: Gordon & Breach), p. 274.

Livingston, W. C. 1969. *Solar Phys.* **7**, 144.

Marcy, G. W. 1984. *Ap. J.* **276**, 286.

Marlborough, J. M. 1969. *Ap. J.* **156**, 135.

Marraco, H. G. & J. C. Muzzio 1980. *Pub. Ast. Soc. Pacific* **92**, 700.

Mathew, A. & R. Rajamohan 1992. *J. Ap. Ast.* **13**, 61.

Mathys, G. 1988. *Ast. Ap.* **189**, 179.

McCarthy, J. K. & L. W. Ramsey 1984. *Ap. J.* **283**, 200.

McLaughlin, D. B. 1924. *Ap. J.* **60**, 22.

    1961. *J. Roy Astron. Soc. Canada* **55**, 13, 73.

Mochnacki, S. W., M. D. Gladders, J. R. Thomson, *et al.* 2002. *Ast. J.* **124**, 2868.

Moss, D. & R. C. Smith 1981. *Rep. Prog. Phys.* **44**, 831.

Noyes, R. W., L. W. Hartmann, S. L. Baliunas, D. K. Duncan, & A. H. Vaughan 1984. *Ap. J.* **279**, 763.

Oke, J. B. & J. L. Greenstein 1954. *Ap. J.* **120**, 384.

Olson, E. C. 1984. *Pub. Ast. Soc. Pacific* **96**, 376.

Penny, L. R. 1996. *Ap. J.* **463**, 737.

Peterson, R. C. 1983. *Ap. J.* **275**, 737.

   1985a. *Ap. J.* **289**, 320.

   1985b. *Ap. J. Lett.* **294**, L35.

Pilachowski, C. A. & R. W. Milkey 1987. *Pub. Ast. Soc. Pacific* **99**, 836.

Plavec, M. J. 1986. *Instrumentation and Research Programmes for Small Telescopes*, ed. J. B. Hearnshaw & P. L. Cottrell. (Dordrecht: Reidel), p. 173.

Poeckert, R. & J. M. Marlborough 1978. *Ap. J.* **220**, 940.

Rebull, L. M., S. C. Wolff, S. E. Strom, & R. B. Makidon 2002. *Ast. J.* **124**, 546.

Reiners, A. & J. H. M. M. Schmitt 2003. *Ast. Ap.* **398**, 647.

Rhode, K. L., W. Herbst, & R. D. Mathieu 2001. *Ast. J.* **122**, 3258.

Rice, J. B. & W. H. Wehlau 1990. *Ast. Ap.* **233**, 503.

   1994. *Pub. Ast. Soc. Pacific* **106**, 134.

Rice, J. B., W. H. Wehlau, & V. L. Khokhlova 1989. *Ast. Ap.* **208**, 179.

Robinson, R. D., S. P. Worden, & J. W. Harvey 1980. *Ap. J. Lett.* **236**, L155.

Rossiter, R. A. 1924. *Ap. J.* **60**, 15.

Roxburgh, I. W. & P. A. Strittmatter 1965. *Z. f. Ap.* **63**, 15.

   1966a. *Mon. Not. Roy. Ast. Soc.* **133**, 1.

   1966b. *Mon. Not. Roy. Ast. Soc.* **133**, 345.

Royer, F., M. Gerbaldi, R. Faraggiana, & A. E. Gómez 2002a. *Ast. Ap.* **381**, 105.

Royer, F., S. Grenier, M.-O. Baylac, A. E. Gómez, & J. Zorec 2002b. *Ast. Ap.* **393**, 897.

Rucinski, S. M. & D. A. VandenBerg 1986. *Pub. Ast. Soc. Pacific* **98**, 669.

Saar, S. H. 1988. *Ap. J.* **324**, 441.

Saar, S. H., J. L. Linsky, & J. M. Beckers 1986. *Ap. J.* **302**, 777.

Sabby, J. A. & C. H. S. Lacy 2003. *Ast. J.* **125**, 1448.

Sandage, A. R. 1955. *Ap. J.* **122**, 263.

Scargle, J. D. 1982. *Ap. J.* **263**, 835.

Schatzman, E. 1962. *Ann. d'Ap.* **25**, 18.

Scherrer, P. H., J. M. Wilcox, & L. Svalgaard 1980. *Ap. J.* **241**, 811.

Schröter, E. H. 1985. *Solar Phys.* **100**, 141.

Shajn, G. & O. Struve 1929. *Mon. Not. Roy. Ast. Soc.* **89**, 222.

Skumanich, A. 1972. *Ap. J.* **171**, 565.

Slettebak, A. 1949. *Ap. J.* **110**, 498.

   1954. *Ap. J.* **119**, 146.

   1955. *Ap. J.* **121**, 653.

   1956. *Ap. J.* **124**, 173.

   1963. *Ap. J.* **138**, 118.

   1966. *Ap. J.* **145**, 126.

   1982. *Ap. J. Suppl.* **50**, 55.

   1985. *Calibration of Fundamental Stellar Quantities*, IAU Symp. 111, ed. D. S. Hayes, L. E. Pasinetti, & A. G. D. Philip. (Dordrecht: Reidel), p. 163.

Slettebak, A. & R. F. Howard 1955. *Ap. J.* **121**, 102.

Slettebak, A., G. W. Collins, II, P. B. Boyce, N. M. White, & T. D. Parkinson 1975. *Ap. J. Suppl.* **29**, 137.

Slettebak, A., T. J. Kuzma, & G. W. Collins, II 1980. *Ap. J.* **242**, 171.

Smith, M. A. & D. F. Gray 1976, *Pub. Ast. Soc. Pacific* **88**, 809.

Smith, M. A., J. M. Beckers, & S. C. Barden 1983. *Ap. J.* **271**, 237.
Soderblom, D. R. 1982. *Ap. J.* **263**, 239.
　1983. *Ap. J. Suppl.* **53**, 1.
　1985. *Ast. J.* **90**, 2103.
Soderblom, D. R., B. F. Jones, & M. F. Walker 1983. *Ap. J. Lett.* **274**, L37.
Soderblom, D. R., B. F. Jones, & D. Fischer 2001. *Ap. J.* **563**, 334.
Stauffer, J. R. 1984. *Ap. J.* **280**, 189.
Stauffer, J. R. & L. W. Hartmann 1987. *Ap. J.* **318**, 337.
Stauffer, J. R., R. A. Schild, S. L. Baliunas, & J. L. Africano 1987. *Pub. Ast. Soc. Pacific* **99**, 471.
Stauffer, J. R., L. W. Hartmann, & B. F. Jones 1989. *Ap. J.* **346**, 160.
Stellingwerf, R. F. 1978. *Ap. J.* **224**, 953.
Stift, M. J. 1986. *Mon. Not. Roy. Ast. Soc.* **221**, 499.
Stoeckley, T. R. 1968. *Mon. Not. Roy. Ast. Soc.* **140**, 121.
Stout-Batalha, N. M. & S. S. Vogt 1999. *Ap. J. Suppl.* **123**, 251.
Strassmeier, K. G., F. C. Fekel, B. W. Bopp, R. C. Dempsey, & G. W. Henry 1990. *Ap. J. Suppl.* **72**, 191.
Strassmeier, K. G. & J. B. Rice 1998. *Ast. Ap.* **330**, 685.
Strassmeier, K. G., D. S. Hall, M. Zeilik, *et al.* 1988. *Ast. Ap. Suppl.* **72**, 291.
Struve, O. 1930. *Ap. J.* **72**, 1.
　1945. *Popular Ast.* **53**, 201.
Sweet, P. A. & A. E. Roy 1953. *Mon. Not. Roy. Ast. Soc.* **113**, 701.
Tassoul, J.-L. 1978. *Theory of Rotating Stars.* (Princeton: Princeton Univ.).
　1987. *Ap. J.* **322**, 856.
　1988. *Ap. J. Lett.* **324**, L71.
Tinker, J., M. Pinsonneault, & D. Terndrup 2002. *Ap. J.* **564**, 877.
Toner, C. G. & D. F. Gray 1988. *Ap. J.* **334**, 1008.
Uesugi, A. & I. Fukuda, 1982. *Revised Catalogue of Stellar Rotation Velocities.* (Kyoto: Kyoto Univ.).
Uitenbroek, H., A. K. Dupree, & R. L. Gilliland 1998. *Ast. J.* **116**, 2501.
Underhill, A. B. & V. Doazan 1982. *B Stars with and without Emission Lines*, CNRS/NASA, NASA SP-456.
van Leeuwnen, F. 1983. Doctoral Thesis, Leiden.
van Leeuwnen, F. & P. Alphenaar 1982. *ESO Messenger* **28**, 15.
Vilhu, O., B. Gustafsson, & B. Edvardsson 1987. *Ap. J.* **320**, 850.
Vogel, S. N. & L. V. Kuhi 1981. *Ap. J.* **245**, 960.
Vogt, S. S. 1983. *Activity in Red Dwarf Stars*, ed. P. B. Byrne & M. Rodono. (Dordrecht: Reidel), p. 137.
Vogt, S. S. & G. D. Penrod 1983. *Pub. Ast. Soc. Pacific* **95**, 565.
Vogt, S. S., G. D. Penrod, & A. P. Hatzes 1987. *Ap. J.* **321**, 496.
von Zeipel, H. 1924. *Mon. Not. Roy. Ast. Soc.* **84**, 665.
Walter, F. M. & G. S. Basri 1982. *Ap. J.* **260**, 735.
Weber, E. J. & L. Davis, Jr. 1967. *Ap. J.* **148**, 217.
Weis, E. W. 1974. *Ap. J.* **190**, 331.
Wilcox, J. M. & R. Howard 1970. *Solar Phys.* **13**, 251.
Wilson, O. C. 1968. *Ap. J.* **153**, 221.
　1978. *Ap. J.* **226**, 379.
Wolff, S. C. 1981. *Ap. J.* **244**, 221.
Wolff, S. C. & J. N. Heasley 1987. *Pub. Ast. Soc. Pacific* **99**, 957.
Wolff, S. C., S. Edwards, & G. W. Preston 1982. *Ap. J.* **252**, 322.
Wolff, S. C., A. M. Boesgaard, & T. Simon 1986. *Ap. J.* **310**, 360.

Questions and exercises

1. Draw the profiles of a spectral line without rotational broadening and with 30 km/s rotational broadening. Have you conserved the equivalent width? Why is the equivalent width not altered by rotation? Now attempt to draw a rotationally broadened profile when the rotation rate is 300 km/s. What special challenges arise when measuring line profiles with very large rotational broadening?

2. How would the rotation profile, $G(\Delta\lambda)$, be altered from the classical case if the star were a rapid rotator showing an elliptical shape (equator-on aspect of view)? If the rotation is rapid enough to significantly distort the shape, then so-called gravity darkening will also come into play, so the equator will be less bright than the poles. Stars can be tricky.

3. A curious secondary phenomenon can be seen in Fig. 18.7. Naturally, the main point of the figure is to illustrate the rotational broadening, but about two-thirds of the way across the field we see that the two lines in the lower panel, when blended together by rotational broadening (upper panel), seem to produce an absorption feature with *three* dips. Interesting. What do you think is happening here?

4. Notice how in Fig. 18.6 you can essentially read off the rotation rates by simply looking at the velocity position of the edges of the profile. This, of course, is simply a reflection of Eq. (18.2), but it is a handy tool to have. Give it a try on the profiles in Figs. 18.8 and 18.10.

5. Investigate the variation in the $v \sin i$ one would derive as a function of assumed limb darkening. Trace the $\varepsilon = 0$ transform in Fig. 18.17 on a transparency (plastic sheet). Be sure to mark the horizontal axis and the 1.0 s/km position. Then translate the sheet and line up the traced transform with the others. While they are lined up, read the ratio of abscissa scales to obtain your answer.

6. In the case illustrated in Fig. 18.3, lines of constant Doppler shift are straight and parallel to the projected rotation axis. What would lines of constant Doppler shift look like if the star had differential rotation, i.e., the angular rotation depended on the stellar latitude?

7. Suppose a rotating star with axis in the plane of the sky has a dark spot $\approx 0.05R$ in size near its equator, where R is the star's radius. Draw three snapshots of a line profile for this star: (i) when the spot is just coming into view from behind the star, (ii) when the spot is at the center of the stellar disk, and (iii) when the spot is halfway between the center of the disk and the limb where it will disappear behind the star. How would your diagrams change with inclination of the rotation axis?